

Accepted Manuscript

Journal of the Geological Society

New geochemical and age constraints ($^{40}\text{Ar}/^{39}\text{Ar}$ and U-Pb) on forearc intrusive rocks from New Caledonia Ophiolite (SW Pacific): diversity of melts generated at hot subduction inception

D. Cluzel, A. Montanini, A. Secchiari, E. Ferrari, M. Heizler, F. Jourdan, S. Meffre, R. Zhou & C. Teyssier

DOI: <https://doi.org/10.1144/jgs2023-145>

To access the most recent version of this article, please click the DOI URL in the line above. When citing this article please include the above DOI.

This article is part of the Ophiolites, melanges and blueschists collection available at: <https://www.lyellcollection.org/topic/collections/ophiolites-melanges-and-blueschists>

Received 31 August 2023

Revised 10 November 2023

Accepted 15 November 2023

© 2023 The Author(s). Published by The Geological Society of London. All rights reserved. For permissions: <http://www.geolsoc.org.uk/permissions>. Publishing disclaimer: www.geolsoc.org.uk/pub_ethics

Supplementary material at <https://doi.org/10.6084/m9.figshare.c.6949265>

Manuscript version: Accepted Manuscript

This is a PDF of an unedited manuscript that has been accepted for publication. The manuscript will undergo copyediting, typesetting and correction before it is published in its final form. Please note that during the production process errors may be discovered which could affect the content, and all legal disclaimers that apply to the journal pertain.

Although reasonable efforts have been made to obtain all necessary permissions from third parties to include their copyrighted content within this article, their full citation and copyright line may not be present in this Accepted Manuscript version. Before using any content from this article, please refer to the Version of Record once published for full citation and copyright details, as permissions may be required.

New geochemical and age constraints ($^{40}\text{Ar}/^{39}\text{Ar}$ and U-Pb) on forearc intrusive rocks from New Caledonia Ophiolite (SW Pacific): diversity of melts generated at hot subduction inception.

New Caledonia Eocene forearc magmatism

D. Cluzel*¹, A. Montanini², A. Secchiari⁴, E. Ferrari²⁻⁴, M. Heizler⁵, F. Jourdan⁶, S. Meffre⁷, R. Zhou⁸ and C. Teyssier⁹

¹ Institut de Sciences Exactes et Appliquées, University of New Caledonia, BP R4 - 98851 Nouméa Cedex, New Caledonia ORCID: 0000-0002-4362-5516

² Department of Chemistry, Life Sciences and Environmental Sustainability, University of Parma, Parco Area delle Scienze 157/a, 43124 Parma, Italy

³ Earth Sciences Dept., University of Milan, Via Botticelli 23 - 20133 Milano, Italy

⁴ Istituto Nazionale di Geofisica e Vulcanologia, Sezione di Milano, Via Alfonso Corti, 12, 20133 Milano, Italy

⁵ New Mexico Institute of Mining & Technology, 801 Leroy Place, Socorro NM 87801-4796, United States

⁶ Western Australian Argon Isotope Facility, John de Laeter Centre & School of Earth and Planetary Sciences, Curtin University, Perth, Australia

⁷ Earth Sciences, University of Tasmania, Sandy Bay Campus, Hobart, Tasmania, Australia.

⁸ School of Earth and Environmental Sciences, The University of Queensland, Brisbane, QLD, Australia

⁹ Earth and Environmental Sciences, 116 Church St SE, University of Minnesota Twin Cities, Minneapolis, MN 55455-2070, United States

* corresponding author dominique.cluzel@unc.nc

Abstract

New Caledonia Ophiolite is crosscut by coarse to medium grained pyroxenites and hornblende gabbros/diorites dykes intruded between 55.5Ma and 50Ma (U-Pb zircon and $^{40}\text{Ar}/^{39}\text{Ar}$ hornblende), while finer-grained dolerites of tholeiitic affinity are younger (50-47 Ma). Production of hornblende-gabbros/diorites was modelled by moderate degree (20-40%) of partial melting of the HT amphibolites of the metamorphic sole. End-member compositions, hornblendites and anorthosites, resulted from solid-state phase segregation of crystal mushes within tectonically active magmatic conduits. Cascade reactions of slab melts with mantle wedge peridotites successively formed clinoenstatite-boninite magmas, which fed gabbronorite cumulate lenses at the mantle-crust

transition, in turn clinoenstatite-boninite melts reacted with peridotites to form websterites. The youngest magmas of tholeiitic affinity, appeared about 6 Ma after subduction inception when the cooler subducting slab plunged more steeply. Incipient slab retreat allowed corner flow, triggering low pressure hydrous melting of the uplifted asthenosphere. The early stages of forearc magmatism were closely associated with transcurrent shear zones, which recorded oblique subduction inception. The lower Eocene tectonic and magmatic features of the New Caledonia ophiolite witness the existence of a north- or northeast-dipping hot (forced) subduction zone in the Southwest Pacific, which appears notably distinct from the slightly younger west-dipping Izu-Bonin-Marianna cold (spontaneous) subduction system.

Keywords : New Caledonia Ophiolite, forearc magmatism, subduction inception, mantle shear zones, $^{40}\text{Ar}/^{39}\text{Ar}$, U-Pb zircon

Introduction

Veins and dykes are commonly found in mantle sections of Supra Subduction Zone (SSZ) ophiolites; they typically are a few centimeters to several meters thick, either with sharp, diffuse, straight or deformed boundaries, and are diversely oriented with respect to the high-temperature peridotite layering. SSZ veins and dykes may have a purely magmatic and partly or totally metasomatic origin. They record a relatively wide range of temperatures and can be emplaced at various stages of ophiolite cooling. Their compositional diversity allows investigation of the various processes that are active in forearc domains of subduction zones (for a review see Furnes and Dilek, 2017). Such investigation is difficult in modern active oceanic forearcs, as these can only be accessed by deep sea drilling. In contrast, SSZ ophiolites that represent obducted forearc lithosphere (e.g., Stern et al., 2008) are easily accessible targets in spite of erosion and tectonic dismantlement.

Pyroxenites are the most common lithologies preserved in the SSZ ophiolite record. Origin of pyroxenite dykes has been attributed to either local harzburgite re-melting (Nicolas, 1989), hydrous melting of depleted mantle wedge peridotites (Xiong et al. 2014), or peridotite-melt interaction (Berly et al., 2006; Rogkala et al., 2017; Le Roux and Liang, 2019) occurring in the early forearc evolution. Owing to their low incompatible elements content, SSZ pyroxenites are generally unsuitable for radio-isotopic dating, and thus rarely constrained temporally. However, some SSZ pyroxenites derived from hydrous melts contain small amounts of magmatic amphibole, which can be dated using the $^{40}\text{Ar}/^{39}\text{Ar}$ method.

Hornblende-rich gabbro/diorite dykes are also common in SSZ ophiolites (Yu et al., 2022). In the New Caledonia (NC) ophiolite, their compositions vary from hornblendite with less than 5% plagioclase, to hornblende gabbro/diorite, and to “anorthosite” (less than 5% hornblende). Unlike other SSZ lithologies, they are sufficiently rich in incompatible elements to develop minerals suitable for geochronology ($^{40}\text{Ar}/^{39}\text{Ar}$ and/or U-Pb). Although of minor importance, biotite-granites/pegmatites occur locally. Basalt dykes commonly occur in SSZ ophiolites; they may be generated early in the forearc history during subduction initiation (Reagan et al., 2010, Hickey-Vargas et al., 2018, Whattam and Stern, 2011; Furnes and Dilek, 2017; Shervais et al., 2019), or later during subduction evolution (e.g., Lallemand and Arcay, 2021 and references therein).

This article presents new structural, geochemical and geochronological data obtained for a set of dykes from the NC ophiolite. These data provide strong constraints on the timing and evolution of forearc magmatism and its relationship to tectonics in the specific case of the inception of a hot and oblique subduction zone. Our new $^{40}\text{Ar}/^{39}\text{Ar}$ amphibole ages from pyroxenite dykes crosscutting the NNE-SSW trending Bogota shear zone and from a synkinematic pyroxenite intrusion associated with NW-SE trending shear zones near Noumea (Plum) provide the opportunity to obtain information not

only on the timing of pyroxenite intrusion, but also on the age of the shearing deformation that affected the host peridotite through the application of the $^{40}\text{Ar}/^{39}\text{Ar}$ method. The widespread occurrence and diversity of magmatic dykes offer new geochronological and geochemical insights into forearc evolution, and more specifically, of a young subduction zone that likely originated at or near a spreading ridge (e.g., Ulrich et al., 2010; Cluzel et al., 2012b).

Material and methods

This study is based on surveys of the Peridotite Nappe conducted from the early 1990s to 2020. Some 125 samples were analyzed for major and trace elements, 23 samples for Nd-Sr isotopes, 30 were selected for U-Pb dating, and 7 for $^{40}\text{Ar}/^{39}\text{Ar}$ dating.

$^{40}\text{Ar}/^{39}\text{Ar}$ dating at Oregon State University. The $^{40}\text{Ar}/^{39}\text{Ar}$ analytical data are organized to comply with FAIR data reporting norms (see for instance Schaen et al., 2020). An Excel workbook is provided with data formatted into individual worksheets with isotope ratio and raw intensity data. Hornblende was separated by standard mineral separation procedures and the samples were irradiated in two packages. NM-312 was at the Oregon State University for 14 hours in the CLICT position, whereas NM-322 was at the USGS reactor in Denver, CO and was for 24 hours. Fish Canyon sanidine was used as the neutron flux monitor and is assigned an age of 28.201 Ma (Kuiper et al., 2008) using a ^{40}K decay constant of $5.463\text{e}^{-10}/\text{a}$ (Min et al., 2000).

After irradiation, the samples were step-heated with a diode laser with a heating time of 45 seconds per step, followed by 60 seconds of gas clean up with a SAES GP-50 getter operated at 1.6 A. Gas was also exposed to a cold finger operated at $\sim -140^\circ\text{C}$. Argon isotopes were measured using a Thermo-Fisher Scientific Helix MC-plus multi-collector mass spectrometer. Isotopes ^{40}Ar , ^{39}Ar , ^{38}Ar , and ^{37}Ar were measured on Faraday collectors with ^{40}Ar and ^{37}Ar using a 10^{12} Ohm resistor, ^{39}Ar using a 10^{13} Ohm resistor, and ^{38}Ar using a 10^{14} Ohm resistor. ^{36}Ar was measured on a compact discrete dynode (CDD) ion counter that has a dead time of 20 ns. CaF_2 and K-glass were included in both irradiations to ensure accurate correction for interfering reactions.

Calibration gases of air and a gas mixture enriched in radiogenic ^{40}Ar along with ^{39}Ar were analyzed interspersed with the samples to monitor instrument drift and determine detector intercalibration factors. Extraction line blanks were interspersed with sample measurements and are reported in the intensity data worksheet. All data collection was conducted with the in-house Pychron software, and data reduction utilized MassSpec version 7.875. The plateau ages are derived from the weighted mean of the chosen steps with the weighting factor being the inverse variance (Taylor, 1982) and the error is the square root of the sum of $1/\sigma^2$ values. Isochron regressions

followed the methods of York (1968). Age errors are reported at 2σ and include the J-factor error and irradiation correction factor uncertainties.

⁴⁰Ar/³⁹Ar dating at Curtin University. We selected two fresh samples of hornblende (VOH 1) and dolerite (SIR 8) for ⁴⁰Ar/³⁹Ar dating. All samples were crushed to centimeter scale using a hydraulic press, after which fresh separates were further crushed to several hundred micrometer in size in a ring mill. The crushates were sieved and washed with deionized water in a sonic bath. Groundmass grains were handpicked from the dolerite sample using a binocular stereomicroscope. For sample VOH1, we isolated amphibole crystals using a Frantz magnetic separator, and then we carefully hand-picked the freshest and inclusion-free crystals under a binocular microscope. The samples were further leached in diluted HF for one minute and then thoroughly rinsed with distilled water in an ultrasonic cleaner.

Samples were loaded into large wells of one 1.9 cm diameter and 0.3 cm depth aluminum disc. These wells were bracketed by small wells that included GA1550 biotite used as a neutron fluence monitor for which an age of 99.738 ($\pm 0.1\%$; 1σ) was adopted (Renne et al., 2011). The discs were Cd-shielded (to minimize undesirable nuclear interference reactions) and irradiated for 3 hours in the US Geological Survey nuclear reactor (Denver, USA) in central position in 2011 and in 2014. The mean J-values computed from standard grains within the small pits range from determined as the average and standard deviation of J-values of the small wells for each irradiation disc is provided in table S6. Mass discrimination was monitored using an automated air pipette relative to an air ratio of 298.56 ± 0.31 (Lee et al., 2006). The correction factors for interfering isotopes were (³⁹Ar/³⁷Ar)Ca = 7.30×10^{-4} ($\pm 11\%$), (³⁶Ar/³⁷Ar)Ca = 2.82×10^{-4} ($\pm 1\%$) and (⁴⁰Ar/³⁹Ar)K = 6.76×10^{-4} ($\pm 32\%$). ⁴⁰Ar/³⁹Ar analyses were carried out in the Western Australian Argon Isotope Facility, at Curtin University, Perth on both a MAP 215-50 (sample VOH1) and ARGUS VI (sample SIR8) mass spectrometers.

Sample VOH1 (hornblende) – a multi-grain aliquot of amphibole crystals was wrapped in low-blank niobium foil and step-heated using a 110 W Spectron Laser Systems, with a continuous Nd-YAG (IR; 1064 nm) laser rastered over the sample for 1 minute to ensure a homogeneously distributed temperature. The gas was purified in a stainless-steel extraction line using two SAES AP10 and one GP50 getters. Ar isotopes were measured in static mode using a MAP 215-50 mass spectrometer (resolution of ~ 500 ; sensitivity of 4×10^{-14} mol/V) with a Balzers SEV 217 electron multiplier using 9 to 10 cycles of peak-hopping. Data acquisition was performed with the Argus program written by M.O. McWilliams and running within a Labview environment. Blanks were monitored every 3 to 4 steps.

Sample SIR8 (dolerite) – small groundmass aliquots were step-heated using a continuous 100 W PhotonMachine© CO2 (IR, 10.6 μ m) laser fired on the aliquot material for 60 seconds. All standard

crystals were measured on the ARGUS VI and fused in a single step. The gas was purified in an extra low-volume stainless steel extraction line of 240 cm³, set up to run with a single SAES AP10 getter. Ar isotopes were measured in static mode using a low-volume (600 cm³) ARGUS VI mass spectrometer from Thermo Fisher© (Jourdan et al., 2019) set with a permanent resolution of ~200. Measurements were carried out in multi-collection mode using three Faraday cups equipped with three 1012 ohm (masses 40; 38; and 37) and one 1013 ohm (mass 39) resistor amplifiers and a low background compact discrete dynode (CDD) ion counter to measure mass 36. We measured the relative abundance of each mass simultaneously during 10 cycles of peak-hopping and 16 seconds of integration time for each mass. Detectors were calibrated to each other through air shot beam signals. Blanks were analyzed for every three to four incremental heating steps.

The raw data (Table S6) were processed using the ArArCALC software (Koppers, 2002), and the ages have been calculated using the decay constants recommended by Renne et al. (2011). All analytical parameters and relative abundance values are provided in Table S6 and have been corrected for blanks, mass discrimination and radioactive decay. Individual errors in Table S6 are given at the 1 σ level. Criteria for the determination of a plateau are as follows: (1) plateaus must include at least 70% of ³⁹Ar; (2) the plateau should be distributed over a minimum of 3 consecutive steps agreeing at 95% confidence level and satisfying a probability of fit (P) of at least 0.05. The use of these criteria means that perturbed spectra are not used for age determination. Plateau ages are given at the 2 σ level and are calculated using the mean of all the plateau steps, each weighted by the inverse variance of their individual analytical error.

U-Pb zircon dating at the University of Tasmania. Twenty representative samples were selected from a set of some 120 dyke samples collected throughout the Peridotite Nappe and dated by LA-ICPMS zircon geochronology at the University of Tasmania.

Approximately 100 g of rock was repeatedly sieved and crushed in a Cr-steel ring mill to a grain size <400 μ m. Non-magnetic heavy minerals were then separated using a gold pan and a Fe-B-Nd hand magnet. The zircons were hand-picked from the heavy mineral concentrate under the microscope in cross-polarised transmitted light. The selected crystals were placed on double sided sticky tape and epoxy glue was then poured into a 2.5 cm diameter mould on top of the zircons. The mount was dried for 12 hours and polished using clean sandpaper and a clean polishing lap. The samples were then washed in distilled water in an ultrasonic bath.

The analyses were performed on Agilent 7500cs quadrupole ICPMS instruments between 2004 and 2015. Data collected prior to 2010 used the New Wave UP193 nm solid state laser equipped with a custom-made laser ablation cell (see Sack et al. 2011 for details). Data collected after 2010 used a 193 nm Coherent Ar-F gas laser and the Resonetics M50 ablation cell. The downhole fractionation,

instrument drift and mass bias correction factors for Pb/U ratios on zircons were calculated using 2 analyses on the primary (91500 standard of Wiendenbeck et al. 1995) and 1 analysis on each of the secondary standard zircons (Temora standard of Black et al. 2003 & JG1 of Jackson et al. 2004) analyzed at the beginning of the session and every 12 unknown zircons (roughly every 1/2 hour) using the same spot size and conditions as used on the samples. Additional secondary standards (The Mud Tank Zircon of Black & Gulson, 1978) were also analysed. The correction factor for the $^{207}\text{Pb}/^{206}\text{Pb}$ ratio was calculated using 3 large spot of NIST610 analysed at the beginning and end of the day and corrected using the values recommended by Baker et al. (2004).

Each analysis on the zircons began with a 30 second blank gas measurement followed by a further 30 seconds of analysis time when the laser was switched on. Zircons were sampled on 32 micron spots using the laser at 5 Hz and a density of approximately 1.5 J/cm^2 . A flow of He carrier gas carried particles ablated by the laser out of the chamber to be mixed with Ar gas and carried to the plasma torch. Elements measured include ^{49}Ti , ^{96}Zr , ^{146}Nd , ^{178}Hf , ^{202}Hg , ^{204}Pb , ^{206}Pb , ^{207}Pb , ^{208}Pb , ^{232}Th and ^{238}U with each element being measured sequentially every 0.16 s with longer counting time on the Pb isotopes compared to the other elements. The data reduction used was based on the method outlined in detail in Meffre et al. (2008) similar to that outlined in Black et al. (2004) and Paton et al (2010). Element abundances in zircons were calculated using the method outlined by Kosler (2001) using Zr as the internal standard element, assuming stoichiometric proportions and using the 91500 to standard correct for mass bias.

U-Pb dating at the University of Queensland. Analyses were performed using a Thermo Fisher iCAP RQ quadrupole inductively coupled plasma mass spectrometer (ICP-MS) equipped with an ASI RESOLUTION SE 193 nm laser at Centre for Geoanalytical Mass Spectrometry (The University of Queensland). Zircon data were collected with a 30 μm spot size in 30 cycles of 1s at a repetition rate of 7Hz and a fluence of 3 J/cm^2 . U-Pb age determinations for zircons were undertaken using the 91500 zircon standard (Wiedenbeck et al., 1995) for background and instrumental bias (Jackson et al., 2004). TEMORA2 (Black et al., 2003) or GJ1 zircons (Jackson et al., 2004) were used as secondary standards to monitor precision and accuracy. Data produced indicate precision and accuracy better than 0.5% for U-Pb age measurements for both analytical sessions. The raw data were processed using the Lolite software (Paton et al., 2011) and later normalized using Zr as the internal standard.

Whole rock and mineral data. Whole-rock major (ICP-OES) and trace-elements (ICP-MS) analyses of hornblende-rich dikes and dolerites were carried out at the CNRS-SARM-CRPG of Nancy (France); analytical procedures, errors and detection limits may be found at <https://sarm.cnrs.fr/index.html>.

Major element mineral analyses of pyroxenites were carried out at Department of Chemistry, Life Sciences and Environmental Sustainability in Parma (Italy) using a JEOL-6400 electron microprobe equipped with a LINK-ISIS energy dispersive micro analytical system. The electron beam was produced at an accelerating voltage of 15 kV and probe current of 0.25 nA. Both natural minerals and synthetic compounds were used as standards.

Geologic setting

The main island of New Caledonia (named Grande Terre) is the emerged northern part of a continent-size area of thinned continental crust termed Zealandia (Luyendyk, 1995; Mortimer et al., 2017), which was rifted from the south Gondwana margin (Antarctica and Australia) during the Late Cretaceous (Hayes and Ringis, 1973). In the northern part of Zealandia, marginal rifting isolated the Norfolk Ridge, a narrow slice of thinned continental crust bound to the west by the New Caledonia Basin and to the east by the proto-Loyalty Basin. New Caledonia geology records a collage of Permian-Mesozoic island-arc related terranes (Meffre, 1995; Aitchison et al., 1995a; Maurizot et al., 2020a) accreted during the late Early Cretaceous and unconformably overlain by a Late Cretaceous-Eocene sedimentary cover (Maurizot et al., 2020b). In turn, pre-Oligocene rocks were tectonically overlain by the obducted oceanic lithosphere of the Loyalty Basin (for details see Cluzel et al., 2012a and Maurizot et al., 2020c).

During the Eocene, the proto-Loyalty Basin was the site of north or northeast dipping intra-oceanic subduction, which resulted in off-scraping of the oceanic lower plate and forearc accretion (Cluzel et al., 2001; Cluzel et al., 2017). Subduction erosion resulted in the formation of serpentinite melange (Cluzel, 2020), while high-pressure low-temperature (HP-LT) metamorphism developed with a northeastward increasing grade (Clarke et al., 1997; Spandler et al., 2005; Vitale Brovarone and Agard, 2013; Maurizot et al., 2020c and references therein). Meanwhile, in-sequence southwest-directed thrusting affected the sedimentary cover of the Norfolk Ridge and generated coeval turbidite basins. Oblique subduction eventually led to arc-continent collision and forearc obduction when the northern tip of the continental Norfolk Ridge blocked the subduction (Aitchison et al., 1995a) at the Eocene-Oligocene boundary (Cluzel et al., 1998).

As a result of Eocene obduction and subsequent erosion, about 5,500 km² of allochthonous upper mantle rocks (Avias, 1967) of the NC Ophiolite, also known as Peridotite Nappe (Paris, 1981), are exposed in the Grande Terre, Belep Island and Isle of Pines (Fig. 1). The Peridotite Nappe is rooted in the Loyalty Basin (Collot et al., 1987) and consists of highly depleted harzburgites (e.g., Nicolas and Prinzhofer, 1983; Marchesi et al., 2009; Pirard et al., 2013; Secchiari et al., 2020), dunites and minor lherzolites (e.g., Ulrich et al., 2010; Secchiari et al., 2016). The ophiolite sheet is up to 2,500 m thick

and is underlain by a serpentinite sole, 20 to 200 m thick. Locally, lenses of high-temperature amphibolites are pinched between the serpentinites and the underlying Poya Terrane (Cluzel et al., 2012b). Near the top of the ultramafic rocks a ~300-500 m thick dunitic transition zone (DTZ) consists of replacive/reactive dunites, which resulted from interaction of olivine-saturated melts with the underlying harzburgites (Marchesi et al., 2009; Pirard et al., 2013). Some wehrlites on top of the DTZ may have a replacive origin as well (Nicolas and Prinzhofer, 1983; Marchesi et al., 2009; Pirard et al., 2013). The DTZ is in turn overlain by mafic-ultramafic cumulate lenses with a distribution, from base to top, of dunites-pyroxenites, wehrlites and websterites-gabbronorites (e.g., Pirard et al., 2013; Secchiari et al., 2018) (Suppl. Fig. S1). The remarkable absence of an upper section of oceanic crust (volcanic rocks and sediments) suggests either deep erosion or removal by intra-crustal tectonic detachment (Cluzel et al., 2001). Notably, the absolute age of the lower crustal intrusive sequence is unknown at present, mainly due to the lack of suitable lithologies for radio-isotopic dating. An upper time constraint of ca. 60 Ma is however provided by Nd model ages of the layered gabbronorites (Secchiari et al., 2018), consistent with their formation during the Early Eocene (Cluzel et al. 2006).

North- or northeast-dipping subduction, which eventually led to obduction, originated within the proto-Loyalty Basin to the east of New Caledonia, which evolved from marginal basin (Late Cretaceous to Paleocene) to forearc setting (Eocene) (Aitchison et al., 1995a, 1995b; Cluzel et al., 2001). Intra-oceanic subduction started shortly before 56 Ma, probably close to a spreading ridge as recorded by U-Pb zircon (55.9 ± 0.8 Ma) and $^{40}\text{Ar}/^{39}\text{Ar}$ amphibole cooling age (55.8 ± 1.7 Ma) of HT amphibolites from the metamorphic sole (Cluzel et al., 2012b; Soret et al., 2016). Obduction occurred after 34 Ma, as constrained by the youngest pre-obduction marine sediments (Cluzel et al., 1998), and before 24.5 Ma, as indicated by post-obduction magmatism (Paquette and Cluzel, 2007). Paleomagnetic data from laterite ferricrete developed upon peridotites suggest that the ophiolite was exposed and subject to weathering for some time before 25 Ma (Sevin et al., 2012).

A variety of dykes displaying supra-subduction geochemical signatures (e.g., Nb-Ta and Ti negative anomalies) crosscut the ophiolite at all levels. These dykes were intruded during the lower Eocene (55.5-50 Ma; U-Pb zircon) (Cluzel et al., 2006) shortly after subduction inception. They are also found dismembered in the porphyroclastic serpentinite sole of the Peridotite Nappe and tectonically mixed with elements of the mafic Poya Terrane, in blueschist and eclogite-facies serpentinite melanges of the Eocene HP-LT belt (Cluzel et al., 2001; Spandler et al., 2005; Cluzel, 2020).

Several high-temperature shear zones crosscut NC ophiolite: the Bogota Transform Fault oriented N20°E (Prinzhofer and Nicolas, 1980; Titus et al., 2011), the Bélep Shear Zone oriented N150°E (Nicolas, 1989; Sécher, 1981; Titus et al., 2011), and the Humboldt Corridor trending N165°E (Ferré et al., 2004; Vogt and Podvin, 1983) (Fig. 1). All these high-temperature shear zones are characterized by steeply dipping foliation and horizontal stretching lineation. No time constraints related to their

activity are currently available so that their correlation with either the Late Cretaceous marginal basin stage or the Eocene fore-arc stage remains speculative.

Tectonics, geochemistry and geochronology of lower Eocene dykes

General features

The majority of dykes that cross-cut the Peridotite Nappe are typically coarse to medium-grained, suggesting they were intruded into relatively hot host rocks. They are found throughout the Peridotite Nappe, regardless of the structural level and nature of the ultramafic host rock (harzburgite, dunite or lherzolite), but they appear more frequent near its base. The dykes are well preserved in the main body of the ultramafic allochthon but are severely disrupted in the serpentinite sole. Blocks of similar supra-subduction magmatic rocks with 55-50 Ma U-Pb zircon ages are found in serpentinite melanges of the HP-LT belt of northern New Caledonia as a result of subduction erosion (Cluzel, 2020).

Widespread coarse-grained felsic dykes suggest relatively slow cooling. In addition, pegmatitic and sub-solvus textures and local formation of retrograde mineral associations suggest the involvement of hydrous fluids during the late- and post-magmatic evolution. Some dykes underwent internal ductile deformation (mineral boudinage, mineral preferred orientation, flow folding or microfolding, mylonitisation), which is not observed in the peridotite host. A compositional layering parallel to dyke walls is locally developed, thus suggesting high-temperature shearing and magma injection in active faults. Two-step intrusion is recorded by some dykes, which display a foliated, earlier, outer part while the rest of the dyke displays granular texture. Shearing therefore only occurred during the early stage of dyke emplacement (Cluzel, 2020) (see outcrop pictures in online appendix, suppl. Figs. S2 and S4).

Due to the large spacing, crosscutting relationships are rarely observed; however, dyke textures allow for establishing a rough chronology. Some dykes display ductile deformation (e.g. Poum Massif, Bogota Peninsula; Titus et al., 2011), thus indicating intrusion within a still hot peridotite. Although coarse-grained, most felsic dykes were emplaced in colder host rocks and developed anthophyllite-chlorite reaction rims or no rims at all. Dolerite/basalt dykes tend to be more common in the upper level of the pile, they show fine-grained texture and locally chilled margins indicating intrusion in cooler host rocks.

Dyke orientations do not fit a simple tension crack model since shallow dipping sills are widespread and two or more sets of upright dykes commonly coexist. At island scale, the dykes roughly cluster at *ca.* N130°E, N20°E, and N70°E; i.e., parallel or perpendicular to the main structural lineaments of the Peridotite Nappe (Cluzel et al., 2021). Magma was injected through joints that likely developed during the cooling of peridotite. For example, dolerite dykes of the Bogota Peninsula, in spite of some dispersion, cluster at *ca.* N20°E (Titus et al., 2011), i.e., roughly parallel to the Bogota Shear Zone (see below).

Sheared dykes are predominantly found near the base of Peridotite Nappe in the south of the island (Plum, Ouen Island, Casy Islet; Fig. 1). They also occur, although less frequently, in northern massifs. Dextral motion is recorded by WNW-ESE trending sheared dykes while rare NNW-SSE trending dykes display sinistral motion, attesting NW-SE directed shortening and NE-SW stretching directions (in the present orientation of the island; Cluzel et al., 2021).

Based on field and major elements classification, dyke compositions vary from ultramafic (pyroxenite) to mafic (gabbro, diorite, hornblendite, dolerite, boninite), and felsic (leucogabbro, leucodiorite, granite) (Fig. 2). Post-magmatic alteration is evidenced in some rocks by the variability of mobile elements and occurrence of secondary mineral phases (tremolite, chlorite, etc). Whole-rock major and trace element analyses of all dyke types (new and published data) are summarized in the online appendix (Suppl. Table S1).

Plum pyroxenite intrusion

The Plum composite intrusion in the Massif du Sud is located E-SE of Noumea near the base of Peridotite Nappe (Fig.1). It includes a sub-circular pyroxenite body about 2 km wide and some smaller elliptical bodies. Besides Upper Oligocene post-obduction granodiorites, it represents the only intrusive body of such size in the Peridotite Nappe. It is intruded in strongly serpentized harzburgites and truncated by the basal thrust, thus providing evidence of subduction erosion (Cluzel, 2020). The intrusion consists of roughly concentric envelopes with dunite, wehrlite, and websterite inwards. The pyroxenite is intruded by hornblende-gabbro dykes oriented either parallel to the curved shape of the intrusion, or perpendicularly crosscutting it (Fig. 3a). Some dykes are sheared and mylonitized (Suppl. Figs. S2c, S2d), especially those oriented NW-SE (Cluzel et al., 2021). The overall Z-shaped structure, with directions changing eastward from E-W to N-S and E-W, and partitioned internal foliation (Suppl. Fig. S2b) suggests synkinematic intrusion in a dextral transcurrent setting (Figs. 3b and 3c).

The main petrographic and geochemical features of the Plum pyroxenite were investigated in detail by Secchiari et al. (2022b). In the following paragraph, the most essential characteristics of these rocks will be summarized. The pyroxenite body consists of medium-grained websterites with magmatic textures ranging from allotriomorphic to orthocumultic. The websterites are mainly composed of orthopyroxene (~ 30–75 vol %) and Al_2O_3 and TiO_2 -poor clinopyroxene (~ 20–50 vol %), coupled to variable amount of amphibole (~ 2–20 vol.%) and minor plagioclase (up to 9 vol.%) with highly calcic composition (An_{88} – An_{96}). Gabbro dykes crosscut the pyroxenite body. In contrast to the pyroxenite core, the dykes are characterized by variable grain size, often showing the concomitant presence of mm-sized crystals (up to 1–2mm) surrounded by a fine-grained (~ 0.1–0.5 mm) crystal matrix. Mineral modes of the dykes are characterized by lower pyroxene contents (Opx ~ 3–40 vol %; Cpx ~ 5–25 vol %) together with higher amphibole and plagioclase abundances (~ 20–30 vol % and ~ 10–55 vol %, respectively) compared to the main pyroxenite body. Pale green amphibole mainly occurs as interstitial phase texturally associated with clinopyroxene. Abundant amphibole blebs, with rounded or irregular margins, are commonly found within clinopyroxene, often in optical continuity with the interstitial amphibole. The amphibole may also form rims on clinopyroxene. According to Secchiari et al. (2022b), the amphibole crystallization may be ascribed to replacement reactions involving the early-crystallized clinopyroxene in a crystal mush environment. Despite the slightly different mineral modes, in situ major element investigation revealed similar compositional features for the pyroxenite core and the crosscutting dykes. Major element pyroxene thermometry (Brey and Kohler, 1990; Taylor, 1998) applied to Plum intrusive rocks provided a temperature interval of 860–955 °C. This temperature range suggests some subsolidus cooling after magmatic crystallization, as evidenced by mutual exsolutions in ortho- and clinopyroxene. The amphibole geothermometer of Putirka (2016) also yields low temperatures (800–910 °C), which are consistent with the late appearance of amphibole in the crystallisation sequence. The pyroxenite intrusion and the associated dykes register similar equilibrium temperatures, thus implying a common cooling history.

The Plum pyroxenites are depleted in incompatible elements and display negative Nb, Zr, Hf, Ta and Ti anomalies on MORB-normalized trace elements diagrams (Fig. 4b). The associated dykes are slightly more depleted and display Eu positive anomalies that suggest plagioclase segregation. Geochemical modelling based on whole-rock and clinopyroxene trace element compositions (Figs. 4a and 4b) indicates that putative melts in equilibrium with the Plum intrusives have a geochemical signature strongly recalling those of the clinoenstatite-bearing (CE) boninites of Népoui (west coast of NC; Secchiari et al., 2022b).

$^{40}\text{Ar}/^{39}\text{Ar}$ ages have been obtained for amphiboles from a websterite (Sample PL-AM7) and a gabbro dyke (PL-AM10) using the step heating technique. According to the classification of Leake et al. (1997) the amphiboles are magnesio-hornblende (Appendix Table S2) characterized by very low K_2O contents (0.10-0.20 wt. %) and high Ca/K ratios (> 50, up to 187). Sample PL-AM7 has an initial step near 58 Ma, older than the remaining steps that yield a flat segment with a well-defined plateau age of 52.3 ± 0.6 Ma (Fig. 5a). PL-AM10 has an overall age pattern that is downward stepping with the majority of the spectrum defined by ages between about 70 to 60 Ma (Fig. 5b). Isochron analysis of the plateau steps for PL-AM7 yields an age equal to the plateau age of 52.5 ± 1.9 Ma along with an initial $^{40}\text{Ar}/^{36}\text{Ar}$ equal to atmospheric argon (Fig. 5c). The isochron array for PL-AM10 yields an age of 53.9 ± 0.6 Ma and reveals an excess argon trapped initial $^{40}\text{Ar}/^{36}\text{Ar}$ of 337.1 ± 1.3 (Fig. 5d) (Appendix Table S3). Based on cross-cutting relationships, the gabbro dyke (PL-AM10) is younger than the websterite (PL-AM7) and the isochron dates are consistent with this as they are analytically indistinguishable at the 2σ level. The $^{40}\text{Ar}/^{39}\text{Ar}$ ages are within the range of U-Pb zircon ages of hornblende-bearing gabbro and diorite dykes (55.6-50.0 Ma) (Cluzel et al., 2006; this study).

Pyroxenite dykelets from the Bogota Peninsula.

The Bogota Peninsula ultramafic rocks represent the NW extension of the Massif du Sud along the northeastern coast of New Caledonia (Fig. 1). The orientation of the peridotite layering varies throughout the Bogota Peninsula from E-W to N-S, dipping 35° to 65° ; a stretching lineation marked by chromite streaks and elongated/boudinaged orthopyroxene grains with a pitch of about 45° in any direction (Fig. 6) is also observed. The moderately dipping layering connects to, or is crosscut by high-temperature dextral shear zones defined by steep mylonitic foliation bearing a shallow dipping lineation (Suppl. Fig. S4c). The main shear zone was interpreted as an ancient oceanic transform and referred to as Bogota Transform Fault (BTF) (Prinzhofer and Nicolas, 1980; Titus et al., 2011). BTF is about 2 km wide around Ouassé Village, while narrower high-strain zones are found elsewhere (Fig. 6); a secondary shear zone was also described 20 km to the NW near Kouaoua Village (Titus et al., 2011).

A number of mafic to ultramafic dykes are distributed throughout the peninsula (Fig. 6). Although they are widely spaced, often preventing crosscutting relationships from being observed, the relative timing from earliest to latest was suggested to be pyroxenite, plagioclase-bearing pyroxenite, hornblende gabbro and dolerite/basalt (Prinzhofer and Nicolas, 1980). Such relative chronology is consistent with decreasing grain size from pyroxenites to basalts, thus suggesting emplacement at decreasing temperature/pressure conditions of the host peridotite.

Depending on their orientation and location within the high-strain domain, pyroxenite dykelets are generally undeformed, post-dating ductile shear deformation of the peridotite. However, some

pyroxenite dykes display ductile shearing or boudinage when parallel to foliation in high strain domains, or ptygmatic folding when perpendicular to it (Titus et al., 2011). Sheared or folded pyroxenite dykes are therefore more or less contemporaneous with transcurrent motion. The orientations of hornblende-gabbro dykes cluster around N5°E, N40°E and N130°E (Fig. 6), broadly consistent with the orientation of dykes in the rest of the ophiolite (Cluzel et al., 2021), bearing no direct relationship to BTF. Finally, undeformed basalt dykes display straight boundaries and cluster around N30°E (Titus et al., 2011). They were seemingly channelized in already cold foliated rock.

In the Ouassé bay (Fig. 6), the pyroxenites occur as 5-15 cm thick dykelets that typically intersect the host peridotite foliation at variable angles (Suppl. Fig. S2d). Rare concordant layers of orthopyroxenites occur as well and some are boudinaged (Suppl. Fig. S2e). Pyroxenites mainly consist of amphibole-bearing (Amp ~5-40 vol. %) websterites and minor orthopyroxenites containing ~5 vol. % of olivine or clinopyroxene. Pyroxenite textures are highly variable, ranging from cumulitic to porphyroclastic or granoblastic-polygonal (Ferrari, 2021). The enclosing harzburgites have textures ranging from porphyroclastic to mylonitic. Their foliation is defined by aligned and/or stretched orthopyroxene, with aspect ratio up to 12:1, and olivine porphyroclasts.

Two hornblendes from websterite samples were dated by the $^{40}\text{Ar}/^{39}\text{Ar}$ method (samples OU1 and OU7B) and consist of orthopyroxene (~25-40 vol%), clinopyroxene (~25 vol%) and light brown amphibole (30-40 vol %). The age spectra are concordant and simple to interpret with sample OU1 yielding a cooling age of 56.01 ± 0.19 Ma, and OU7B gave an analytically identical age of 56.05 ± 0.17 Ma (Fig. 7; Appendix Table S3), without any evidence for partial degassing or excess argon.

The sample OU1 displays a disequigranular texture with medium- to coarse-grained pyroxenes set into a fine-grained granoblastic polygonal matrix composed of pyroxenes + amphibole and accessory amounts of Ca-rich plagioclase and Cr-spinel. Conversely, sample OU7B has a coarse-grained cumulitic texture with interstitial/poikilitic amphibole and accessory apatite and Fe-Ni sulfides. Pyroxene geothermometry of Brey and Köhler (1990) and Taylor (1998) applied to pyroxenites provided temperatures between 920-990°C. Consistent values (970 °C) were obtained using the amphibole-plagioclase thermometer of Holland and Blundy (1994). Ca-in-orthopyroxene method applied to the the porphyroclastic (920-970°C) and neoblastic (925-945°C) assemblage of the adjacent harzburgites yielded comparable temperature estimates (Ferrari, 2021).

Recently, Xu et al. (2021) proposed that the websterites from the Ouassé bay resulted from migration of boninitic melts into the host harzburgite. However, trace element composition of the calculated melts in equilibrium with clinopyroxene of the amphibole websterites of this work are distinctly enriched in incompatible elements with respect to boninitic melts and are similar to high-Mg adakites (Ferrari, 2021). By contrast, the orthopyroxenite-forming liquids have a boninitic affinity (Fig. 4c and 4d).

The dated amphiboles are analogous in chemistry to those dated from Plum pyroxenite intrusion (Appendix, Table S2), i.e. they are magnesio-hornblendes with low TiO_2 (0.68-1.21 wt%) and K_2O contents of 0.15 and 0.28 wt%. They have nearly identical $^{40}\text{Ar}/^{39}\text{Ar}$ cooling ages of 56.05 ± 0.17 Ma and 56.01 ± 0.19 Ma respectively (Fig. 7) without any evidence for partial degassing or excess argon.

The two pyroxenite occurrences (Plum and Ouassé) partly differ by chemical composition, structure, size and, to some extent, their timing. The Ouassé samples are measurably older than the Plum samples at the 2σ confidence level. The slightly older one (Ouassé) is associated with the HT Bogota shear zone. Here, the emplacement of different types of pyroxenite-forming liquids (boninites and high-Mg adakites) was contemporaneous or closely followed ductile deformation. The age of 56 Ma places the genesis of Ouassé pyroxenites and ductile shearing at the onset of subduction. The apparently younger Plum pyroxenites occurred in much larger bodies and were dominated by more depleted parental magmas, yet they were also associated with large-scale transcurrent tectonics.

Nepoui clinoenstatite-boninite and boninite-series dykes

Boninite outcrops from Plaine des Gaiacs, referred to as Nepoui clinoenstatite (CE)-boninite (Fig. 1), have been extensively studied since their discovery (Sameshima et al., 1983). Reassessment of these outcrops has shown that Nepoui CE-boninite consists of blocks enclosed within the serpentinite sole of Peridotite Nappe together with other dismembered magmatic rocks (Cluzel et al., 2016). The mineralogical and geochemical features of the Nepoui boninite were already described in detail (Sameshima et al., 1983; Cameron et al., 1983; Cameron, 1989; Ohnenstetter and Brown, 1996; Solovova et al., 2012) and are outlined here. The Nepoui boninite displays hyaloporphyritic texture with some 50–60% dark glassy groundmass including poly-synthetically twinned clinoenstatite, orthopyroxene (bronzite) and olivine microphenocrysts, and accessory clinopyroxene, hornblende and chromite. Clinoenstatite laths, a diagnostic component of boninites, 1–4 mm long, contain minute chromite grains and appear as decussate aggregates.

The Nepoui boninites have andesitic major elements composition ($\text{SiO}_2 = 55.5$ wt.%, $\text{Al}_2\text{O}_3 = 10.0$ wt.% on av. for 10 samples) with low CaO (3.8 wt.% on av.) and FeO contents (7.6 wt.%), low CaO/ Al_2O_3 ratio (0.4 on av.), very low K_2O (0.6 wt.%) and TiO_2 (0.2 wt.%). In contrast, they display high MgO (11–15 wt.%) and high contents in compatible elements contents (Cr = 486–1371 ppm, Ni = 190–1640 ppm) (Cluzel et al., 2016).

In contrast with the classical U-shaped REE pattern of boninites of the type locality (Bonin islands; Crawford et al., 1998; Shervais et al., 2022), Nepoui CE-boninites display slightly concave “spoon-

shaped" REE patterns with significant LREE enrichment ($(La/Sm)_N=2.2$; Fig. 4a), which are similar to that of the less REE-depleted boninites from Cape Vogel (Walker and Cameron, 1983; König et al., 2010; Kamenetsky et al., 2002; Cluzel et al., 2016). According to the classification scheme of Pearce and Reagan (2019), they diagnostically plot in the domain of high-silica boninites (Suppl. Fig. S4a). On the expanded incompatible trace elements diagram normalized to N-MORB, they exhibit a well-defined negative anomaly in Nb, Ta and Ti and a positive anomaly in Zr and Hf very similar to the patterns of Cape Vogel boninites. In contrast, Nepoui boninites exhibit slightly higher incompatible elements, more pronounced Ti negative anomalies (Cluzel et al., 2016; Fig. 4b) and lower contents in compatible elements compared to Cape Vogel boninites.

Based on multi-element geochemical modeling Cluzel et al. (2016) proposed that Nepoui CE-boninites derived from a moderately depleted mantle rock modified by low degree partial melts of a mafic source similar to the BABB-like amphibolites of the metamorphic sole. Remarkably, the calculated melting residue strongly differs from the ultra-depleted harzburgites of Peridotite Nappe, ruling out that these harzburgites represent the mantle residue left after boninites extraction.

$^{40}Ar/^{39}Ar$ dating of glassy fragments yielded Early Eocene cooling ages (47.4 ± 0.9 Ma and 50.4 ± 1.3 Ma) (Cluzel et al., 2016). Considering the glassy character of the rock, the older age is likely to approach the emplacement age.

Numerous dykes within the Peridotite Nappe exhibit geochemical features akin to those observed in the Nepoui CE-boninites, i.e. REE contents, high-MgO, negative Nb, Ta and Ti anomalies, positive Zr and Hf anomalies (Figs. 4e and 4f), and were referred to as boninite-series by Cluzel et al. (2016). However, none of them are *sensu stricto* boninites and they dominantly plot in the domain of high-Mg andesites on the classification diagram of Pearce and Reagan (2019) (Suppl. Fig. S5). Although no modeling was performed for these rocks, a process similar to that of CE-boninites may be postulated for their origin; i.e. partial melting from a mantle source modified by slab melts (e.g. Wood and Turner, 2009). U-Pb zircon dating of these rocks provided a narrow age range between 54.5 ± 0.7 Ma and 53.2 ± 0.6 Ma (Cluzel et al. 2016), within the age range of the other dykes of the Peridotite Nappe.

Hornblende-bearing dykes and hornblendites

Hornblende-gabbro and diorite dykes are common in ophiolites from various tectonic settings. In New Caledonia they occur at all levels of the ophiolite but decrease in frequency from the base to the top of the Peridotite Nappe. Their compositions vary from hornblendite (with less than 5% plagioclase) to leucocratic anorthosite (less than 5% hornblende) through hornblende gabbro/diorite. Many hornblende-bearing dykes display structures that record high- to medium-temperature deformation compatible with transcurrent kinematics (Cluzel et al., 2021). Textures such as

amphibole prisms with preferred orientation, compositional layering, isoclinal folding, sigmoidal stretched amphibole grains and mylonitic fabrics suggest a syn- to late-magmatic deformation of the dykes (Suppl. Figs. S3c and S3d). The host peridotites do not display any sign of similar ductile deformation that could be coeval to these textures suggesting that the hydrous magmas were injected in active faults in a transcurrent tectonic setting (Cluzel et al., 2021). Hornblendite samples display slight LREE depletion (Fig. 8a) with hook-shaped patterns typical of amphibole-dominated modal compositions (Henderson, 1984). In the REE and trace elements MORB-normalized diagram these samples display Nb, Ta and Ti negative anomalies diagnostic of subduction-related magmas (Fig. 8b). Zircon U-Pb (50 ± 3 Ma; Suppl. Fig. S5a) and hornblende $^{40}\text{Ar}/^{39}\text{Ar}$ dating (54.9 ± 2.8 Ma; Suppl. Fig. S5b) of representative hornblendite samples (RPYR 6 and VOH 1 respectively, Appendix Table S4 and S5) consistently indicate lower Eocene ages, which are within uncertainty of each other.

The chemistry of hornblende-gabbro/diorite dykes shows higher incompatible elements abundances with respect to hornblendites, with positive and negative Eu anomalies, systematic negative Nb, Ta and Ti anomalies, and Zr-Hf positive anomalies (Fig. 8c and 8d). Variable high-field strength elements (HFSE) depletion in many hornblendites and hornblende gabbro/diorite samples (Fig. 8b and 8d) are consistent with the occurrence of residual garnet in their sources. U-Pb dating of zircons from 12 samples provides crystallization ages from 55.7 ± 1.3 Ma to 52.3 ± 0.9 Ma with an average of ca. 54 Ma (Suppl. Fig. S6) (Appendix Table S4). These new data are consistent within error with the previously published average of 53 Ma (Cluzel et al., 2006); however, in detail, such older average value accounts for the new sampling of the middle and northern parts of Peridotite Nappe where dykes are slightly older than in Massif du Sud (see discussion below).

Anorthosite dykes are light-colored rocks sharply contrasting in the field with the host peridotite. They form cm- to m-thick coarse to medium-grained dykes that represent the leucocratic (amphibole-poor) end-member of the hydrous rock suite. They typically show variable REE contents with slightly U-shaped patterns, some of which are much depleted, with a prominent Eu positive anomaly (Fig. 8e) that suggest plagioclase accumulation. However, the positive Eu anomaly does not increase together with decreasing bulk REE content, suggesting that plagioclase enrichment did not occur by fractional crystallization solely. In contrast, plagioclase, and in counterpart, hornblende enrichment may result from solid-state mineral segregation within crystal mushes. Examples of mineral segregation within dykes are particularly well exposed in Ouen Island where a compositional layering (Suppl. Fig. S3e) is isoclinally folded in some internally deformed dykes (Suppl. Fig. S3f). The occurrence of compositional layering and hornblendite and anorthosite enclaves within the same gabbro dyke (Suppl. Figs. S3g and S3h) are evidence for their cogenetic character. Therefore, it is suggested that solid-state segregation of plagioclase in anorthosites represents the counterpart of

amphibole enrichment in hornblende. Due to the low Zr content (2-100 ppm) zircons are rare in these rocks and only samples with $Zr > 60$ ppm could be dated. Zircons from sample NFC 4 yielded a U-Pb age of 52.6 ± 0.4 Ma (Appendix Suppl. Fig. S7, Table S4); i.e. within the age range as the bulk of lower Eocene dykes.

Granites

Biotite and quartz-bearing felsic dykes are not uncommon in the Peridotite Nappe and similarly to other dyke types display various textures, from granular to pegmatitic, due to relatively slow cooling. They typically contain 71-78.7 wt% SiO_2 , 12.3-15.3 wt% Al_2O_3 , 3.7-6.7 wt% Na_2O+K_2O , low K_2O (0.1-2 wt%) and low FeO and MgO contents (Appendix Table S1) plotting in the granite field of the TAS diagram (Le Bas et al., 1986; Le Maitre et al., 2002; Fig. 2). The sample OUEN 3 differs by its extreme depletion in some incompatible elements (e.g. $Na_2O+K_2O = 0.81$) and HREE. Samples KO6 and KO11 display higher K_2O contents (4.4-4.7 wt%). On the REE diagram normalized to the chondrite C1 (Evensen et al., 1978) two kinds of patterns are distinguished: type 1) spoon-shaped patterns with or without Eu anomalies, and type 2) slightly U-shaped patterns with or without Eu anomalies (Fig. 8g). The sample OUEN 3 (type 1) displays an extreme depletion in HREE and a prominent Eu positive anomaly. On the REE and trace elements diagram normalized to N-MORB (Fig. 8h), the type 1 granites display variable Nb-Ta negative anomalies and Zr-Hf positive anomalies and the type 2 does not display Nb-Ta anomalies. Type 1 granites display trace-elements patterns typical of adakite series and their similarities with hornblende-bearing dykes likely denote a similar origin through a lesser melting degree and/or fractionation. In contrast, the U-shaped REE patterns of type 2 granites strongly recall that of boninite series rocks, although they are not boninites sensu stricto (Appendix Fig. S5). Similarly to the other dykes except dolerites, their U-Pb zircon ages define a narrow range between 54.2 Ma and 53.1 Ma (Appendix Fig. S7 and Table S4).

Dolerite dykes

Dolerite dykes 1-10 m thick, are relatively rare in the Peridotite Nappe and a crosscutting relationship with other dykes was never observed; however, microcrystalline texture and occurrence of chilled margins suggest intrusion in an already cold peridotite and late emplacement compared to other dyke types. Dolerite dykes are oriented $N20^\circ E$ on average (Titus et al., 2011; Cluzel et al., 2021), suggesting brittle NW-SE-directed extension at the time of dolerite intrusion.

The dolerite samples examined in this study were taken from various locations, including the Massif du Sud (Montagne des Sources, Tontouta, and Dumbea river valleys) and the west coast massifs (Boulinda, Tiebaghi). As such, they provide a representative overview of the entire Peridotite Nappe. The analyzed samples are basalts or basaltic andesites (Fig. 9a) that display LREE depletion similar to MORB in chondrite-normalized diagrams (Fig. 9b). They also have variable but prominent negative anomalies in Nb and Ta and weakly negative Ti anomalies normalized to N-MORB (Fig. 9d). These features and Hf-Th-Ta relationships (Wood, 1980; Vermeesch, 2006; Fig. 9c) allow a classification as island arc tholeiites (IAT). Only one sample that displays a negative slope on C1-normalized REE diagram plots in the Island arc basalt (IAB) domain of the Hf-Th-Ta diagram (Fig. 9c).

A K-Ar age of 50 Ma was previously reported for a dolerite crosscutting a cumulate lens at Montagne des Sources (Massif du Sud) (Paris, 1981), but no analytical data were provided in this work. One dolerite dyke from Boulinda Massif (Si Reis nickel mine) was selected for $^{40}\text{Ar}/^{39}\text{Ar}$ dating (SIR 8, this study). This sample is one of the most primitive in the dolerite sample set (Fig. 9b) and indicated a cooling age of 50.4 ± 0.2 Ma (Fig. 10) (Appendix Table S6).

A dredge on the top of continental slope a few km to the west of Koumac (DR4, IPOD program) collected vitric and vesicular volcanic rock fragments embedded in a late Pliocene micritic matrix, the location of which was judged enigmatic by the authors (Mortimer et al., 2018). This rock, classified as andesite based on Nb/Y ratio (Fig. 9a), has 'immobile' trace-elements features (Nb-Ta and Ti negative anomalies, Hf/Th and Th/Ta ratios) that place it in the domain of island-arc tholeiite series, similar to the low Nb/Y IAT dykes of Peridotite Nappe (Figs. 9c and 9d). Poorly defined $^{40}\text{Ar}/^{39}\text{Ar}$ apparent ages of 40-48 Ma (Mortimer et al., 2018) may be interpreted as minimum ages due to marine alteration and low-temperature Ar loss, and make it a probable differentiated product of the Eocene IAT magmas. We suggest that these rocks, along with similar, though undated rocks reported from the western New Caledonia margin (Mortimer et al., 2018), were first emplaced at a shallow level of the Peridotite Nappe, or erupted on its top and later collapsed onto the continental slope.

Andesites from the Intermediate Melange

The Intermediate Melange of northern New Caledonia consists of elongate serpentinite mélange lenses that contain various rock types, including blocks of serpentinitized harzburgites, dolerites, basalts, cherts and leucocratic rocks (Cluzel, 2020). These lenses, 5 to 50 km long, are pinched within Diahot Terrane schists and display the same greenschist/blueschist to lower eclogite HP-LT metamorphism and foliation attitude. The material of this melange was scraped off from both the Poya Terrane (accreted in front of, and beneath the forearc) and from the mantle wedge (serpentinitized peridotites and dismembered dykes, see Cluzel, 2020).

The Haute Néhoué Unit is a large block (ca 1 km-wide) within the melange, located at the northwestern end of an 11 km-long NW-SE trending melange sliver, which contains smaller blocks of Poya Terrane basalts, dolerites, red cherts, felsic rocks and deeply serpentinized harzburgites enclosed in a sheared serpentinite matrix. Haute Néhoué Unit consists of a coherent set of mafic and intermediate rocks in tectonic contact with isoclinally folded Late Cretaceous black cherts and Paleocene micrite of the Diahot Terrane in the south, and with Poya Terrane basalt blocks and Late Cretaceous black cherts to the north (see Cluzel, 2020 for details). It is composed of greenish pillow lavas and medium-grained felsic dykes. Geochemical classification based upon immobile trace elements ratios (Zr/TiO_2 , Nb/Y) (Winchester and Floyd, 1977) delineate one single fractionation trend from andesitic basalt to dacite (diorite) composition for these rocks (Suppl. Fig. S8a). Chondrite-normalized REE patterns display moderate LREE enrichment and flat HREE patterns with moderate positive and negative Eu anomalies denoting some plagioclase accumulation and fractionation respectively (Suppl. Fig. S8b and S8c). Parallel REE and incompatible trace elements patterns suggest origin from a common parental melt via moderate degree of fractionation. The most evolved dyke (medium-grained diorite #NHE10) yielded a U-Pb zircon age of 54.7 ± 0.8 Ma (Cluzel, 2020), indicating that the andesitic sequence is coeval with the earliest dykes of the Peridotite Nappe.

Inherited zircons

With the exception of the diorite dyke of the Haute Néhoué Unit, in which the occurrence of 23% inherited zircon grains (at 978, 435, 139 and 129 Ma; Cluzel, 2020) signals contamination by crustal rocks or, more probably, clastic sediments (late Cretaceous ?) and despite the large number of zircons analyzed from Lower Eocene magmatic rocks, no zircon older than 55.5 Ma was found in the 25 representative dyke samples dated by the U-Pb method. We thus infer that neither crustal rock nor clastic sediment was involved in the genesis of Lower Eocene dykes of Peridotite Nappe.

Nd-Sr, Hf and oxygen isotope geochemistry

Representative samples of the various dyke types were analyzed for Sr and Nd isotopes at the CNRS isotope facility of the Laboratoire Magmas et Volcans, University of Clermont-Ferrand, France) (see appendix for details). Apart for a minor trend toward higher $^{87}Sr/^{86}Sr$ ratios likely due to low-T alteration, all dyke types display Sr-Nd isotope signatures close to Depleted MORB Mantle (DMM). In particular, ϵ_{Nd} values recalculated at 54 Ma vary between 6.33 and 10.12 (Appendix Table S7 and Fig. 11). This precludes the involvement of continental crust or sedimentary material, in agreement with the absence of xenocrystic zircons or older zircon cores (see above and Xu et al., 2021). Remarkably, amphibolites of the metamorphic sole yielded similar values ($7.11 < \epsilon_{Nd} < 10.04$; avg.=8.50), which may

indicate some genetic relationship (Fig. 11). Nd-Sr isotope ratios of dolerites ($7.41 < \epsilon_{Nd} < 9.36$; avg.=8.8) are consistent with their tholeiitic (IAT) composition.

Hafnium isotope signature of zircons from gabbro and diorite blocks from the serpentinite sole ($9.4 < \epsilon_{Hf} < 12.9$) (Xu et al., 2021) are also consistent with the origin from a DMM-type source.

However, the oxygen isotope composition of zircons ($+4.74\text{‰} < \delta^{18}\text{O} < +6.63\text{‰}$) suggest minor involvement of subduction-related aqueous fluids in magma genesis (Xu et al., 2021).

Discussion

The tectonic and geochemical features of the lower Eocene dyke system raise issues and provide clues on the geodynamic setting of New Caledonia Ophiolite and the shear zones that crosscut it.

The transform fault setting of HT shear zones questioned

The current paleotransform interpretation of Belep and Bogota shear zones, which are thought to connect laterally with the mantle fabric of Peridotite Nappe (Maurizot et al., 2020c), suggests the occurrence of differently oriented spreading ridge segments (Suppl. Fig. 9a), a common feature of back-arc basins (e.g., North Fiji Basin, Auzende et al., 1995) and could account for oroclinal bending of the northernmost part of Norfolk/New Caledonia Ridge (Northern D'Entrecasteaux Ridge) (Cluzel et al., 2021). However, their geometric relationships do not match those of transform fault system of multiple ridge basins (see Fig. 1). Alternatively, NW-SE (Belep) and NNE-SSW trending (Bogota) dextral shear zones could correspond to C and C' shears respectively, related to regional transcurrent tectonics (e.g., Finch et al., 2020 and references therein; Suppl. Fig. 9b). This interpretation better fits the dextral transcurrent tectonics marked by km-scale "Z-folds" with vertical axes that preceded obduction in the Eocene HP-LT belt and in the Poya Terrane as well (Cluzel et al., 2021). It is worth noting that the occurrence of sheared gabbro dykes re-injected by the same magma, dated at ca 54 Ma, which remained undeformed indicates the initiation of such tectonic regime in the upper plate at the beginning of the 55.5-50.0 Ma time interval (Cluzel et al., 2021). Similarly, undeformed pyroxenite dykelets of the Bogota shear zone dated at ca 56 Ma, which postdate ductile motion, were intruded immediately after subduction inception at ≥ 56 Ma. Hence, a syn-subduction transcurrent tectonics interpretation for the development of these high-T shear zones seems more likely. The presence of syn-kinematic orthopyroxenite dikes derived from boninite melts in the Bogota shear zone, reinforces such interpretation. Transcurrent tectonics occurring at subduction inception is consistent with an induced (forced) subduction (Stern, 2004), which may overcome the

buoyancy of the hot oceanic lithosphere when intra-oceanic subduction starts at or near a spreading center.

The occurrence of high-temperature shear zones now situated a few tens to hundreds of meters above the basal thrust of the ophiolite (i.e. the exhumed roof of the Eocene subduction zone), and reworked supra-subduction dykes in the serpentinite melange, point toward subduction erosion (Cluzel, 2021) and fast uplift along the subduction channel. This interpretation is also supported by the cooling rate calculated for mantle wedge peridotites (Secchiari et al., 2022a) and Lu-Hf garnet age constraints obtained from exhumed eclogites of the Pouebo Terrane (~38 Ma, Taetz et al., 2021). Both lines of evidence point to fast cooling (10-100°C/Myr and 50°C/Myr respectively) and high exhumation rates ($7 \cdot 10^3$ m/Myr).

Genesis of hornblende-gabbro/diorite dykes; a modeling approach.

With the exception of extreme compositions, all hornblende-bearing dykes share some geochemical features, i.e., LREE/HREE enrichment with moderate (e.g. Gd/Yb up to 3.5, suppl. Table S1), low Y, prominent Nb-Ta negative anomalies, variable Ti negative anomalies and Zr(-Hf) positive anomalies (Fig. 8) that argue for the presence of amphibole, garnet and rutile as residual minerals in their sources. Overall, these geochemical signatures are typical of adakites found in subduction zone settings worldwide. However, the Sr/Y ratios of most Lower Eocene hornblende dikes vary in a wide range (Fig. 12 and Appendix Table S1). Only 30% of the analyzed samples have Sr/Y > 40 and could be therefore recognized as adakites s.s. according to the original definition of Defant and Drummond (1990). Taking into account the less restrictive classification proposed by Richards and Kerrich (2007), up to ~60% of the samples can be considered as adakite-like rocks (Sr/Y > 20) derived from the partial melting of a mafic source. The variable Sr/Y ratios and HREE depletion of gabbro/diorite dykes may be viewed as a consequence of the variable amounts of garnet in their source (e.g., Moyen, 2009).

The HT amphibolites of the metamorphic sole of the NC Ophiolite could be viewed as proxy of the slab source of hornblende dike-forming melts. Overall, MORB-type Nd isotope signatures of these HT amphibolites are consistent with the compositions of hornblende gabbro/diorite dikes (Fig. 11). Melting modeling was therefore attempted using the trace-elements composition of the BABB-type amphibolites of the metamorphic sole (Cluzel et al., 2012b; Fig. 13a) and partition coefficients of Bédard (2006) modified by Zhang et al. (2013) (Appendix Table S8). The best fit results were obtained with a protolith containing 5 wt% garnet, 70 wt% amphibole, 20 wt% plagioclase, 3% titanite and 1% rutile for an equilibrium melting rate of 20-40%. Owing to the variability of amphibolites of the

metamorphic sole, end-member compositions were used in the calculation (Hi and Lo in Fig. 13a). The majority of the hornblende-diorite/gabbro dikes fall in the range of model melts (Fig. 13b), with some variability of LILEs and Ti contents though. While Ti may be controlled by retention of rutile and its different proportions in the source rocks, the prominent Rb (and K, not shown) variability/depletion in the investigated hornblende dykes most likely results from post-solidus (hydrothermal) elemental mobility.

A significant number of hornblende diorite/gabbro dikes (as listed in Supplementary Table S1) exhibit higher MgO (8.4-13.2 wt%) than typical adakites (MgO = 3-6 wt%, Defant and Drummond, 1990; Richards and Kerrich, 2007), or than melts with intermediate silica contents experimentally obtained from dehydration melting of amphibolite (Rapp and Watson, 1995). Such chemical features are frequently coupled with high compatible trace element contents (e.g. $300 \text{ ppm} < \text{Cr} < 3500 \text{ ppm}$), which point to interaction of slab-derived melts with an ultramafic component (Rapp et al., 1999; Martin et al., 2005). Mixing with a peridotite-derived component, either through melt/rock interaction (Rapp et al., 1999; Prouteau et al., 2001) or melting of a peridotite source metasomatized by silicic slab melts (Martin et al., 2005) may partly obscure/overprint pristine adakitic signatures, lowering initially high Sr/Y and La/Yb ratios.

Notably, most hornblendites and anorthosites strongly diverge from the major element composition of hornblende gabbro/diorites. However, they generally retain similar trace element (e.g. Nb, Ta, Ti negative anomalies) and Sr-Nd isotope signatures. These rocks have mineralogical and textural features such as hornblende cracks filled with plagioclase, hornblende/anorthosite layering (Appendix Supplem. Figs. S3e and S3f) and the occurrence of comagmatic anorthosite and hornblende enclaves within hornblende-gabbro dykes (Appendix Suppl. Figs. S3g and S3h), which suggest that these rocks formed by the segregation of solid mineral phases from crystal mushes originating from similar melts as hornblende diorite/gabbros dykes.

The switch to IAT and the thermal regime of subduction

The late occurrence (~ 50Ma) of tholeiitic dykes with subduction signatures (IAT) coeval with the end of slab melt production suggests a change in the thermomechanical regime of the subduction zone. Slab cooling after subduction inception took about 12 Ma to evolve from the HT-LP gradient close to the spreading ridge (56 Ma) to the HP-LT gradient recorded by eclogites at 44 Ma (Spandler et al., 2005). Petrochronological studies performed on the Semail Ophiolite, which share some analogies with New Caledonia, have shown that the intra-oceanic subduction zone remained warm for about 5 My after subduction inception (Soret et al., 2022), a time span comparable to the duration of slab melting in NC. After that, eclogitization of the mafic crust increased its density and provoked the

acceleration of subduction, slab steepening and corner flow. Meanwhile, slab dehydration that followed the cessation of slab melting (e. g., Mibe et al., 2011) induced hydrous melting of the uplifted asthenosphere and generated IAT dykes in the upper plate.

Evolution of melts generated at subduction inception

The prominent diversity of dykes generated at subduction inception suggests the occurrence of at least five different melt series:

- “Direct” slab melts formed by low-degree partial melting of the HT amphibolites (hornblende-gabbro/diorite series) variably influenced by an ultramafic component. Hornblendites and anorthosites represent end-members of solid-phase separation within magmatic conduits;
- Melts derived from moderately depleted mantle wedge peridotites modified by slab melts (CE-boninite), which in turn, generated gabbro cumulates
- Melts generated by hydrous melting of mantle wedge peridotites modified by CE-boninite melt (hornblende-pyroxenites, websterites);
- Tholeiitic melts derived from “fertile” mantle sources that intruded an already cooled host rock (IAT dolerites);
- Andesites formed by hydrous melting of undepleted peridotite with some sediment contribution.

The geochemistry of the pyroxenite dykes shows that they were likely generated from hydrous melting of moderately depleted harzburgite previously modified by slab melt inputs, similar to the parental magma of the CE-boninite. The local New Caledonia harzburgites are too depleted to be the melting residue of these melts (Cluzel et al., 2016; Secchiari et al, 2022b) indicating a different mantle source. The volumetrically predominant hornblende-gabbro/diorite dykes are likely to have been mostly slab-sourced and were intruded during the whole episode of forearc magmatism (55.5 Ma to 50 Ma). The end of this episode of slab melting that recorded slab cooling at ~50 Ma coincided with the occurrence of mantle-sourced IAT dolerites. Therefore, the ophiolite of New Caledonia belongs to a minor group of supra-subduction ophiolites in which the magmatic activity is dominated by adakite-like rocks that resulted from partial melting of the subducting slab (Furnes and Dilek, 2017).

Magmatic rocks that erupted or intruded in the forearc soon after subduction inception in the interval 56-50 Ma generally do not display any discernable evolution through time (e.g., Mg# and Sr/Y; other elemental ratios not presented) (Suppl. Figs. S10a and S10b); except an increase of the

Th/Ta ratio and negative Nb (and Ta) anomaly (Suppl. Figs. S10c and S10d), which both record an increasing influence of amphibole in the source rock through time. There is only a small difference in the timing of dyke intrusion along strike the island. Dyke emplacement started at ~54 Ma on average in the northern (west coast) massifs vs. ~ 53Ma in Massif du Sud (Supplem. Fig. S11a). Such diachronism suggests that subduction was not only oblique at start, but also progressed southward in a fan-like fashion due to the bending of the retreating slab (Supplem. Fig. S11b). This feature is consistent with the Eocene anticlockwise rotation of New Caledonia recorded by paleomagnetic data (Cluzel et al., 2021).

Subducted sediments did not contribute to the genesis of slab melts because the basalts of the lower plate that recrystallized to generate the amphibolites of the metamorphic sole, source of slab melts, were too young to carry sediments. When sediments transported by the lower plate (i.e., the Norfolk Ridge) finally entered the subduction zone, the HP-LT thermal regime was already established and led to eclogite crystallization instead of partial melting.

The origin of andesitic pillow lavas erupted on the sea floor above the subduction zone at 54.0 ± 1.0 Ma (Cluzel, 2020) is an unusual feature at hot subduction inception, i.e. before the corner flow is established. It could be postulated that lower Eocene andesites resulted from the differentiation of IAT magma; however, their REE and trace elements contents are drastically different (Fig. 9 and Suppl. Fig. S8); in addition, the IAT dykes have significantly higher Hf/Th ratios (>3) that rule out contamination by continental crust or clastic sediments. It is suggested that andesites originated from the melting of a previously metasomatized mantle source uplifted locally due to transcurrent tectonics (transtension) in a subsidiary forearc basin. The occurrence of inherited zircon grains in the cogenetic diorite dyke (Cluzel, 2020) signals contamination by crustal rocks crosscut by the ascending magma or, more likely, subducted Late Cretaceous clastic sediments, which are a significant component of the HP-LT belt (Diahot Terrane).

The dating and geochemistry outlined in this study show that melting occurred in a variety of different sources over a relatively short period of time with a large predominance of slab melts. Although the context is somewhat different (intra-oceanic subduction vs. active margin), these results meet in part the conclusions of Kimura et al. (2014) based upon the late Cenozoic volcanism of SW Japan associated with the subduction of the young Shikoku Basin. Accordingly, forearc magma diversity is due to the interaction of slab melts with diverse sources, as also proposed by Yu et al. (2020) for the west Philippine ophiolites, where the first magmatic products vary from normal to enriched MOR-type basalts, with no boninite occurrence. This finding does not fit the 'subduction initiation rule' (SIR; Whattam and Stern, 2011), which was established from the western Pacific Izu-

Bonin-Mariana (IBM) subduction. In the IBM system and some Tethyan-type ophiolites (e.g. Dilek and Thy, 2009; Shervais et al., 2019, 2021; Coulthard et al., 2021), forearc basalts erupted first, followed by boninites before the transfer of the magmatic activity into the volcanic arc itself. Similarly, the progressive magmatic evolution of the NC ophiolite does not follow the typical sequence predicted for the supra-subduction type ophiolite by Dilek and Furnes (2011), i.e. N-MORB, IAT and boninites, exemplified by the Jurassic Albanides-Hellenides ophiolites (Saccani et al., 2018).

Differences between the IBM system and the sequence of events in the Early Eocene to the east of New Caledonia indicate different subduction initiation mechanism. The IBM arc is thought to have been established from the onset of subduction in a “cold” old Western Pacific plate. In contrast, Eocene subduction in New Caledonia started near a spreading center and involved young, hot and buoyant oceanic lithosphere (Cluzel et al., 2012a, 2020). Hence, the conditions necessary to generate forearc basalts at subduction onset were not met. Tholeiitic basalt dykes (IAT) were emplaced 6 myr after subduction inception, when the down-going plate was sufficiently cold for eclogites to form, which would have increased the slab bulk density and associated steepening. This may have resulted in the incipient retreat of the slab, allowing mantle upwelling and generation of IAT. Afterwards, the magmatic activity was probably transferred into the volcanic arc itself (the Loyalty Arc) and magma generation in the forearc ceased.

This evolution hypothesis challenges the correlation of NC and IBM subduction zones proposed by many authors (e.g. Whattam et al., 2008, Mortimer et al. 2018, Agranier et al., 2023). In detail, these subduction zones differ on several key points: i) subduction inception in NC and IBM was only roughly synchronous, with NC subduction starting before 56 Ma; i.e., circa 4-5 myr before IBM subduction initiation at 51-52 Ma (Reagan et al., 2013; Ishizuka et al., 2018); ii) NC subduction was hot and shallow-dipping at the beginning and may be considered as forced subduction. In contrast, IBM involved old and cold western Pacific lithosphere, was steeply dipping and likely spontaneous (i.e. gravity-driven); iii) IBM subduction zone was (and is still) plunging continent-ward (i.e., W-ward), while NC subduction originally plunged ocean-ward (i.e., N- or NE-ward after mid-Eocene anticlockwise rotation).

Conclusion

Lower Eocene dykes in the New Caledonian Peridotite Nappe dominantly originated from slab melts generated by low-pressure melting of high-temperature amphibolites. There was no sensible evolution of magmatic activity through time except an increase of amphibole signature in the source, probably by metamorphic disequilibrium of clinopyroxene. All lithotypes occurred throughout the period except IAT dolerites that appeared in the final stage and intruded already cooled mantle

wedge rocks. Slab melts formed at relatively low pressure (garnet-poor source rock) from the still hot and shallow-dipping slab; in contrast, IAT appeared by the end of the forearc magmatic activity and record the change into progressively cooler and more steeply dipping subduction zone (Fig. 14a). Most slab melts were emplaced directly and cooled relatively slowly, while some interacted with the mantle wedge peridotites and indirectly generated CE-boninite. In turn, CE-boninites and coeval melts interacted with peridotites and were responsible for the formation of websterite intrusive rocks (Figs. 14b and 14c). The melts were generated in the forearc of a shallow-dipping and hot subduction zone, which originated near a spreading ridge at ca 56 Ma, progressively cooled, and then plunged more steeply at ca 50 Ma (Fig. 14a). The bulk of forearc magmatism occurred during that short time interval. Such an evolution is at odds with the forearc basalt-then-boninite sequence suggested by the SIR; thus it seems that the sequence eruption in hot and shallow (forced) subduction zones such as the north- or northeast-dipping Eocene subduction of New Caledonia differs markedly from that in colder subduction zones such as the Izu-Bonin-Marianna system.

Acknowledgements

Most of analytical work presented in this study benefited from the financial support of the University of New Caledonia (1992-98 and 2008-2020) and University of Orleans (1999-2007) to DC. AM's travel and living costs during her stay in New Caledonia were supported by a grant of UNC Research Council to DC (R40107_2018). This work has benefited from the equipment and framework of the COMP28 HUB and COMP-R Initiatives, funded by the 'Departments of Excellence' program of the Italian Ministry for Education, University and Research (MIUR, 583 2018-2022 and MUR, 2023-2027).

Data availability

The datasets generated during and/or analysed during the current study are available in the [NAME] repository, []

References

- Agranier A., Patriat M., Mortimer N., Collot J., Etienne S., Durance P., Gans Ph., the VESPA team, 2023. Oligo-Miocene subduction-related volcanism of the Loyalty and Three Kings ridges, SW Pacific: a precursor to the Tonga-Kermadec arc. *Lithos* 436-437, 106981. <https://doi.org/10.1016/j.lithos.2022.106981>
- Aitchison, J.C., Clarke, G.L., Cluzel, D., Meffre, S., 1995a. Eocene arc-continent collision in New Caledonia and implications for regional Southwest Pacific tectonic evolution. *Geology* 23, 161–164. [https://doi.org/10.1130/0091-7613\(1995\)023<0161:EACCIN>2.3.CO;2](https://doi.org/10.1130/0091-7613(1995)023<0161:EACCIN>2.3.CO;2)
- Aitchison, J.C., Meffre, S., Cluzel, D., 1995b. Cretaceous/Tertiary radiolarians from New Caledonia Geological Society of New Zealand, Miscellaneous Publication. 81A, 70.
- Auzende J.-M., Pelletier B., and Eissen J.-P., 1995. The North Fiji Basin : geology, structure and geodynamic evolution. In : Taylor B. (Ed.) Back-arc Basin : tectonics and magmatism. Plenum Press, New York, 139-175.
- Avias J., 1967. Overthrust structure of the main ultrabasic New Caledonian massives. *Tectonophysics*, 4, 531-541, [https://doi.org/10.1016/0040-1951\(67\)90017-0](https://doi.org/10.1016/0040-1951(67)90017-0)
- Baker, J., Peate, D., Waight, T. and Meyzen, C., 2004. Pb isotopic analysis of standards and samples using a Pb-207-Pb-204 double spike and thallium to correct for mass bias with a double-focusing MC-ICP-MS. *Chemical Geology* 211, 275-303. <https://doi.org/10.1016/j.chemgeo.2004.06.030>
- Bédard, J.H., 2006. A catalytic delamination-driven model for coupled genesis of Archaean crust and sub-continental lithospheric mantle. *Geochimica et Cosmochimica Acta* 70, 1188–1214. <http://doi.org/10.1016/J.GCA.2005.11.008>
- Berly, T. J., Hermann, J., Arculus, R. J., and Lapierre, H. 2006. Supra-subduction zone pyroxenites from San Jorge and Santa Isabel (Solomon Islands). *Journal of Petrology*, 47(8), 1531-1555. <http://dx.doi.org/10.1093/petrology/egl019>
- Black L.P., Gulson B.L., 1978. The age of the Mud Tank carbonatite, Strangways Range, Northern Territory. *BMR J Aust Geol Geophys* 3,227–232.
- Black L.P., Kamo S.L., Allen C.M., Aleinikoff J.N., Davis D.W., Korsch R.J., Foudoulis C., 2003. TEMORA 1: a new zircon standard for Phanerozoic U-Pb geochronology. *Chemical Geology* 200, 155-170. [https://doi.org/10.1016/S0009-2541\(03\)00165-7](https://doi.org/10.1016/S0009-2541(03)00165-7)
- Black L.P., Kamo S.L., Allen C.M., Davis D.W., Aleinikoff J.N., Valley J.W., Mundil R., Campbell I.H., Korsch R.J., Williams I.S., Foudoulis C., 2004. Improved ²⁰⁶Pb/²³⁸U microprobe geochronology by the monitoring of a trace-element-related matrix effect; SHRIMP, ID-TIMS, ELA-ICP-MS and oxygen isotope documentation for a series of zircon standards. *Chemical Geology* 205, 115-140. <https://doi.org/10.1016/j.chemgeo.2004.01.003>

- Brey G.P., and Köhler T., 1990. Geothermobarometry in four-phase Iherzolites II. New thermobarometers, and practical assessment of existing thermobarometers. *Journal of Petrology*, 31, 1353-1378 <https://doi.org/10.1093/petrology/31.6.1353>
- Cameron W.E., McCulloch M.T., and Walker D.A., 1983. Boninite petrogenesis: Chemical and Nd-Sr isotopic constraints. *Earth and Planetary Science Letters* 65, 1, 75-89. [https://doi.org/10.1016/0012-821X\(83\)90191-7](https://doi.org/10.1016/0012-821X(83)90191-7)
- Cameron, W.E., 1989. Contrasting boninite–tholeite associations from New Caledonia. In: Crawford, A.J. (Ed.), *Boninites and Related Rocks*. Unwin Hyman, London, 314–338.
- Chang, Z., Vervoort J. D., McClelland W. C., and Knaack C., 2006. U-Pb dating of zircon by LA-ICP-MS, *Geochem. Geophys. Geosyst.*, 7, Q05009, <https://doi.org/10.1029/2005GC001100>
- Clarke G., Aitchison J.C. and Cluzel D., 1997. Eclogites and blueschists of the Pam Peninsula, NE New Caledonia: a reappraisal. *Journal of Metamorphic Petrology* 38, 7, 843-876. <https://doi.org/10.1093/etroj/38.7.843>
- Cluzel D., Chiron D. et Courme M.D., 1998. Discordance de l'Eocène supérieur et événements pré-obduction en Nouvelle-Calédonie (Pacifique sud-ouest) *Comptes Rendus Académie des Sciences Paris*, 327: 485-91. [http://dx.doi.org/10.1016/S1251-8050\(99\)80077-9](http://dx.doi.org/10.1016/S1251-8050(99)80077-9)
- Cluzel D., Aitchison J.C., Picard C., 2001. Tectonic accretion and underplating of mafic terranes in the Late Eocene intraoceanic fore-arc of New Caledonia (Southwest Pacific). *Geodynamic implications*. *Tectonophysics* 340, 1-2, 23-60. [https://doi.org/10.1016/S0040-1951\(01\)00148-2](https://doi.org/10.1016/S0040-1951(01)00148-2)
- Cluzel D., Meffre S., Maurizot P., and Crawford A.J., 2006. Earliest Eocene (53 Ma) convergence in the Southwest Pacific; evidence from pre-obduction dikes in the ophiolite of New Caledonia. *Terra Nova.*, 18, 395-402. <https://doi.org/10.1111/J.1365-3121.2006.00704.X>
- Cluzel D., Maurizot P., Collot J. and Sevin B., 2012a. An outline of the Geology of New Caledonia; from Permian-Mesozoic Southeast-Gondwanaland active margin to Tertiary obduction and supergene evolution. *Episodes* 35, 1, 72-86. <https://doi.org/10.18814/epiiugs/2012/v35i1/007>
- Cluzel D., Jourdan F. Meffre S., Maurizot P., and Lesimple S. 2012b. The metamorphic sole of New Caledonia ophiolite; $^{40}\text{Ar}/^{39}\text{Ar}$, U-Pb, and geochemical evidence for subduction inception at a spreading ridge. *Tectonics*. 31, 3, <https://doi.org/10.1029/2011TC003085>
- Cluzel D., Ulrich M., Jourdan F., Paquette J.L., Audet M.A., Secchiari A., and Maurizot P., 2016. Early Eocene clinostatite boninite and boninite-series dikes of the ophiolite of New Caledonia; a witness of slab-melt enrichment of the mantle wedge in a nascent volcanic arc. *Lithos* 260, 429-442. <https://doi.org/10.1016/j.lithos.2016.04.031>
- Cluzel D., Whitten M., Meffre S., Aitchison J.C., Maurizot P., 2017. A reappraisal of the Poya Terrane (New Caledonia). Accreted Late Cretaceous marginal basin upper crust, passive margin sediments and Eocene E-MORB sill complex. *Tectonics* 37, 1, 48-70. <https://doi.org/10.1002/2017TC004579>

- Cluzel D., 2020. Subduction erosion; contributions of footwall and hanging wall to subduction melange; field, geochemical and radiochronological evidence from the Eocene HP-LT belt of New Caledonia. *Australian Journal of Earth Sciences* 68, 1, 99-119
<https://doi.org/10.1080/08120099.2020.1761876>
- Cluzel D., Iseppi M., and Chen Y., 2021. Eocene pre- and syn-obduction tectonics in New Caledonia (Southwest Pacific). A case for oblique subduction, transcurrent tectonics and oroclinal bending; structural and paleomagnetic evidence. *Tectonophysics* 811, 228875
<https://doi.org/10.1016/j.tecto.2021.228875>
- Collot, J. Y., Malahoff, A., Recy, J., Latham, G., and Missegue, F. 1987. Overthrust emplacement of New Caledonia Ophiolite: Geophysical evidence. *Tectonics* 6, 3, 215-232.
<https://doi.org/10.1029/tc006i003p00215>
- Compston W., 1999. Geological age by instrumental analysis: the 29th Hallimond Lecture. *Mineral Mag.* 63, 297-311. <https://doi.org/10.1180/002646199548475>
- Coulthard, D. A., Reagan, M. K., Shimizu, K., Bindeman, I. N., Brounce, M., Almeev, R. R., et al., 2021. Magma source evolution following subduction initiation: Evidence from the element concentrations, stable isotope ratios, and water contents of volcanic glasses from the Bonin forearc (IODP expedition 352). *Geochemistry, Geophysics, Geosystems*, 22, e2020GC009054.
<https://doi.org/10.1029/2020GC009054>
- Crawford A.J., Falloon T.J. and Green D.H., 1998. Classification, petrogenesis and tectonic setting of boninites. In: *Boninites and related Rocks*, A.J. Crawford Ed. ISBN 978-004445003, 1-49. Unwin and Hyman London
- Defant, M.J. and Drummond, M.S., 1990. Derivation of some modern arc magmas by melting of young subducted lithosphere. *Nature*, 347, 662-665. <https://doi.org/10.1038/347662a0>
- Dilek Y., and Thy P., 2009. Island arc tholeiite to boninitic melt evolution of the Cretaceous Kizildag (Turkey) ophiolite: Model for multi-stage early arc-forearc magmatism in Tethyan subduction factories. *Lithos* 113, 68-87. <http://doi.org/10.1016/j.lithos.2009.05.044>
- Dilek, Y., Furnes, H., 2011. Ophiolite Genesis and Global Tectonics: Geochemical and Tectonic Fingerprinting of Ancient Oceanic Lithosphere. *Geological Society of America Bulletin*, 123, 387-411. <https://doi.org/10.1130/B30446.1>
- Evensen, N.M., Hamilton, P.J., O'Nions, R.K., 1978. Rare earth abundance in chondritic meteorites. *Geochimica et Cosmochimica Acta* 42, 1199-1212. [https://doi.org/10.1016/0016-7037\(78\)90114-X](https://doi.org/10.1016/0016-7037(78)90114-X)
- Ferrari E., 2021. Mantle heterogeneities in rifting-related and supra-subduction settings: examples from External Ligurian and New Caledonia Ophiolites. PhD thesis, University of Parma, 149p.

- Ferré, E.C., Belley, F., Tikoff, B., Martín-Hernández, F., Nzokwe, G. and Ward, C., 2004. Anatomy of an oceanic mantle shear zone deduced from high-field magnetic anisotropy: the Humboldt corridor, New Caledonia. *Eos Trans. AGU*, 85(47), Fall Meeting Supplement, Abstract GP23B-04.
- Finch M.A., Bons P.D., Steinbach F., Grier A., Llorens M.-G., Gomez-Rivas E., Rana H., de Riese T., 2020. The ephemeral developments of C' shear bands: A numerical modelling approach. *Journal of Structural Geology* 139, 104091 <https://doi.org/10.1016/j.jsg.2020.104091>
- Fryer B.J., Jackson S.E., and Longerich H.P., 1993. The application of laser ablation microprobe-inductively coupled plasma-mass spectrometry (LAM-ICP-MS) to in situ U-Pb geochronology. *Chemical Geology* 109, 1-4, 1-8. [https://doi.org/10.1016/0009-2541\(93\)90058-Q](https://doi.org/10.1016/0009-2541(93)90058-Q)
- Furnes H., and Dilek, Y., 2017. Geochemical characterization and petrogenesis of intermediate to silicic rocks in ophiolites: A global synthesis. *Earth-Science Reviews* 166, 1-37. <http://dx.doi.org/10.1016/j.earscirev.2017.01.001>
- Harley S.L. and Kelly N.M., 2007. Zircon Tiny but Timely. *Elements* 3 (1), 13–18. <https://doi.org/10.2113/gselements.3.1.13>
- Hayes D.E. and Ringis J., 1973. Seafloor spreading in the Tasman Sea. *Nature* 243, 454-458. <https://doi.org/10.1038/243454a0>
- Hickey-Vargas R., Yogodzinski G.M., Ishizuka O., McCarthy A., Bizimis M., Kusano Y., Savov I.P., Arculus R., 2018. Origin of depleted basalts during subduction initiation and early development of the Izu-Bonin-Mariana island arc: Evidence from IODP expedition 351 site U1438, Amami-Sankaku basin. *Geochimica et Cosmochimica Acta* 229, 85–111. <https://doi.org/10.1016/j.gca.2018.03.007>
- Holland T. and Blundy J., 1994. Non-ideal interactions in calcic amphiboles and their bearing on amphibole-plagioclase thermometry. *Contributions to Mineralogy and Petrology* 116, 433-447. <https://doi.org/10.1007/BF00310910>
- Ishizuka, O., Hickey-Vargas R., Arculus, R., Yogodzinski, G.M., Savov, I.P., Kusano, Y., McCarthy, A., Brandl, P.A. Sudo, M., 2018, Age of Izu–Bonin–Mariana arc basement, *Earth and Planetary Science Letters* 481, 80-90, <https://doi.org/10.1016/j.epsl.2017.10.023>
- Jackson, S.E., Pearson, N.J., Griffin, W.L., and Belousova, E.A., 2004. The application of laser ablation-inductively coupled plasma-mass spectrometry to in situ U–Pb zircon geochronology. *Chemical Geology* 211, 47-69. <https://doi.org/10.1016/j.chemgeo.2004.06.017>
- Jourdan, F., Nomade, S., Wingate, M.T., Eroglu, E. and Deino, A., 2019. Ultraprecise age and formation temperature of the Australasian tektites constrained by $^{40}\text{Ar}/^{39}\text{Ar}$ analyses. *Meteorit Planet Sci* 54, 2573-2591.
- Kamenetsky V.S, Sobolev A.V, Eggins S.M, Crawford A.J, and Arculus R.J, 2002. Olivine-enriched melt inclusions in chromites from low-Ca boninites, Cape Vogel, Papua New Guinea: evidence for

- ultramafic primary magma, refractory mantle source and enriched components. *Chemical Geology* 183, 1–4, 287–303. [https://doi.org/10.1016/S0009-2541\(01\)00380-1](https://doi.org/10.1016/S0009-2541(01)00380-1)
- Kimura, J.-I., Gill J.B., Kunikiyo T., Osaka I., Shimoshioiri Y., Katakuse M., Kakubuchi S., Nagao T., Furuyama K., Kamei A., Kawabata H., Nakajima J., van Keken P.E., and Stern R.J., 2014. Diverse magmatic effects of subducting a hot slab in SW Japan: Results from forward modeling, *Geochem. Geophys. Geosyst.*, 15, 691–739, <https://doi.org/10.1002/2013GC005132>
- König, S., Münker, C., Schuth, S., Luguet, A., Hoffmann, J.E., Kuduon, J., 2010. Boninites as windows into trace element mobility in subduction zones. *Geochimica et Cosmochimica Acta* 74, 684–704. <http://dx.doi.org/10.1016/j.gca.2009.10.011>
- Koppers, A.A.P., 2002. ArArCALC - software for Ar-40/Ar-39 age calculations. *Comput Geosci-Uk* 28, 605–619.
- Košler J., and Sylvester P., 2003. Present trends and the future of zircon in geochronology: laser ablation ICPMS. *Reviews in Mineralogy & Geochemistry* 53 (1), 243–275. <https://doi.org/10.2113/0530243Corpus>
- Košler, J., 2001. Laser-ablation ICPMS study of metamorphic minerals and processes. In: Sylvester P. J. ed. *Laser-ablation-ICPMS in the earth sciences; principles and applications Mineralogical Association of Canada Short Course Handbook 2001*, 29, 185–202.
- Kuiper, K. F., Deino A., Hilgen, F. J., Krijgsman, W., Renne, P. R., and Wijbrans, J. R., 2008. Synchronizing the rock clocks of Earth history. *Science* 320, 500–504 <https://doi.org/10.1126/science.1154339>
- Lallemand S. and Arcay D., 2021. Subduction initiation from the earliest stages to self-sustained subduction: Insights from the analysis of 70 Cenozoic sites. *Earth-Science Reviews* 221, 103779 <https://doi.org/10.1016/j.earscirev.2021.103779>
- Le Bas, M.J., Le Maitre, R.W., Streckeisen, A. and Zanettin, B., 1986. A Chemical Classification of Volcanic Rocks Based on the Total Alkali-Silica Diagram. *Journal of Petrology*, 27, 745–750. <https://doi.org/10.1093/petrology/27.3.745>
- Le Maitre R. W. (editor), A. Streckeisen, B. Zanettin, M. J. Le Bas, B. Bonin, P. Bateman, G. Bellieni, A. Dudek, S. Efremova, J. Keller, J. Lamere, P. A. Sabine, R. Schmid, H. Sorensen, and A. R. Woolley, 2002. *Igneous Rocks: A Classification and Glossary of Terms, Recommendations of the International Union of Geological Sciences, Subcommittee of the Systematics of Igneous Rocks.* Cambridge University Press, 2002. ISBN 0-521-66215-X
- Le Roux V. and Liang Y., 2019. Ophiolitic pyroxenites record boninite percolation in subduction zone mantle. *Minerals* 9, 565. <https://doi.org/10.3390/min9090565>
- Leake, B. E., Woolley, A. R., Arps, C. E. S., Birch, W. D., Gilbert, M. C., Grice, J. D., Hawthorne, F. C., Kato, A., Kisch, H. J., Krivovichev, V. G., Linthout, K., Laird, J., Mandarino, J. A., Maresch, W. V.,

- Nickel, E. H., Rock, N. M. S., Schumacher, J. C., Smith, D. C., Stephenson, N. V. N., Ungaretti, L., Whittaker, E. J. W. & Youzhi, G., 1997. Nomenclature of amphiboles. *American Mineralogist* 82, 1019-1037. <https://doi.org/10.1180/minmag.1997.061.405.13>
- Lee, J.Y., Marti, K., Severinghaus, J.P., Kawamura, K., Yoo, H.S., Lee, J.B. and Kim, J.S., 2006. A redetermination of the isotopic abundances of atmospheric Ar. *Geochimica Cosmochimica Acta* 70, 4507-4512. <https://doi.org/10.1016/j.gca.2006.06.1563>
- Luyendyk, B., 1995, Hypothesis for Cretaceous rifting of East Gondwana caused by subducted slab capture. *Geology* 23, 373-376, [https://doi.org/10.1130/0091-7613\(1995\)023<0373:HFCROE>2.3.CO;2](https://doi.org/10.1130/0091-7613(1995)023<0373:HFCROE>2.3.CO;2)
- Marchesi C., Garrido C.J., Godard M., Belley F., and Ferré E., 2009. Migration and accumulation of ultra-depleted subduction-related melts in the Massif du Sud ophiolite (New Caledonia). *Chemical Geology* 266, 171–186 <https://doi.org/10.1016/j.chemgeo.2009.06.004>
- Martin H., Smithies R.H., Rapp R., Moyen J.-F., Champion D., 2005. An overview of adakite, tonalite–trondhjemite–granodiorite (TTG), and sanukitoid: relationships and some implications for crustal evolution. *Lithos* 79, 1-24. <http://doi.org/10.1016/j.lithos.2004.04.048>
- Maurizot P., D. Cluzel, S. Meffre, H. J. Campbell, J. Collot and B. Sevin, 2020a. Chapter 3: Pre-Late Cretaceous basement terranes of the Gondwana active margin of New Caledonia. Geological Society, London, Memoirs 51, 27-52. <https://doi.org/10.1144/M51-2016-11>
- Maurizot P., A. Bordenave, D. Cluzel, J. Collot and S. Etienne, 2020b. Chapter 4: Late Cretaceous to Eocene cover of New Caledonia: from rifting to convergence. In: Maurizot P., and Mortimer, N. (ed.). *New Caledonia: Geology, Geodynamic Evolution and Mineral Resources*. Geological Society, London, Memoirs 51, 53–91, <https://doi.org/10.1144/M51-2017-18>
- Maurizot, P., Cluzel, D., Patriat, M., Collot, J., Iseppi, M., Lesimple, S., Secchiari, A., Bosch, D., Montanini, A., Macera, P., and Davies, H.L., 2020c. Chapter 5: The Eocene Subduction-Obduction Complex of New Caledonia. In: Maurizot P., and Mortimer, N. (ed.). *New Caledonia: Geology, Geodynamic Evolution and Mineral Resources*. Geological Society, London, Memoirs 51, <https://doi.org/10.1144/M51-2018-70>
- Meffre, S., 1995. The development of island-arc related ophiolites and sedimentary sequences in New Caledonia. PhD thesis, University of Sydney, Australia, 258 pp.
- Meffre S., Large R.R., Scott R., Woodhead J., Chang Z., Gilbert S.E., Danyushevsky L.V., Maslennikov V., Hergt J.M., 2008. Age and pyrite Pb-isotopic composition of the giant Sukhoi Log sediment-hosted gold deposit, Russia. *Geochimica et Cosmochimica Acta* 72, 2377–2391. <https://doi.org/10.1016/j.gca.2008.03.005>

- Mibe K., Kawamoto T., Matsukage K.N., Fei Y., and Ono S., 2011. Slab melting versus slab dehydration in subduction-zone magmatism. *Proc. Natl. Acad. Sci. USA* 108, 20, 8177-8182. <https://doi.org/10.1073/pnas.1010968108>
- Min, K., Mundil, R., Renne, P. R. and Ludwig, K. R., 2000. A test for systematic errors in $^{40}\text{Ar}/^{39}\text{Ar}$ geochronology through comparison with U–Pb analysis of a 1.1 Ga rhyolite. *Geochimica Cosmochimica Acta* 64, 73–98. <https://doi.org/10.1016/S0016-7037%2899%2900204-5>
- Mortimer N., Campbell H. J., Tulloch A. J., King P. R., Stagpoole V. M., Wood R. A., Rattenbury M. S., Sutherland R., Adams C. J., Collot J., Seton M., 2017. Zealandia: Earth's Hidden Continent. *GSA Today* 27, 3, 27–35 <https://doi.org/10.1130/GSATG321A.1>
- Mortimer N., Gans P.B., Meffre S., Martin C. E., Seton M., Williams S., Turnbull R. E., Quilty P.G., Micklethwaite S., Timm C., Sutherland R., Bache F., Collot J., Maurizot P., Rouillard P., Rollet N., 2018. Regional volcanism of northern Zealandia: post-Gondwana break-up magmatism on an extended, submerged continent. *Geological Society, London, Special Publications* 463, 1, 199-226 <http://dx.doi.org/10.1144/SP463.9>
- Moyen J.F., 2009. High Sr/Y and La/Yb ratios: The meaning of the “adakitic signature”. *Lithos* 112, 3–4, 556-574. <https://doi.org/10.1016/j.lithos.2009.04.001>
- Nicolas, A. and Prinzhofer, A., 1983. Cumulative or residual origin for the transition zones in ophiolites, structural evidence. *Journal of Petrology*, 24, 188-206. <http://dx.doi.org/10.1093/petrology/24.2.188>
- Nicolas, A., 1989. *Structure of Ophiolites and Dynamics of Oceanic Lithosphere*. Dordrecht, Kluwer Academic Publishers, 367 p.
- Ohnenstetter, D., and Brown, W.L., 1996. Compositional variation and primary water contents of differentiated interstitial and included glasses in boninites. *Contributions to Mineralogy and Petrology* 123, 117–137. <https://doi.org/10.1007/s004100050146>
- Paquette, J.L. and Cluzel, D., 2007. U–Pb zircon dating of post-obduction volcanic-arc granitoids and a granulite-facies xenolith from New Caledonia. Inference on Southwest Pacific geodynamic models. *International Journal of Earth Sciences (Geol. Rundsch.)* 96, 613–622. <https://doi.org/10.1007/s00531-006-0127-1>
- Paris, J.-P., 1981. *Géologie de la Nouvelle-Calédonie; un essai de synthèse*. Mémoire du B.R.G.M. 113, ISSN 0071-8246 Orléans, France, 278 p.
- Paton C., Woodhead J.D., Hellstrom J.C., Hergt J.M., Greig A., Maas R., 2010. Improved laser ablation U–Pb zircon geochronology through robust downhole fractionation correction. *Geochemistry, Geophysics, Geosystems* 11, 3. <https://doi.org/10.1029/2009GC002618>
- Pearce, J.A., and Reagan, M.K., 2019. Identification, classification, and interpretation of boninites from Anthropocene to Eoarchean using Si–Mg–Ti systematics: *Geosphere* 15, 4, 1008-1037. <https://doi.org/10.1130/GES01661.1>

- Pirard C., Hermann J., O'Neill H.S.C., 2013. Petrology and geochemistry of the crust-mantle boundary in a nascent arc, Massif du Sud Ophiolite, New Caledonia, SW Pacific. *Journal of Petrology* 54, 1759–1792 <https://doi.org/10.1093/PETROLOGY/EGT030>
- Prinzhofer, A., and Nicolas, A., 1980. The Bogota peninsula, New Caledonia: A possible oceanic transform fault. *Journal of Geology* 88, 387-398, <https://doi.org/10.1086/628523>
- Prouteau, G., Scaillet, B., Pichavant, M., Maury, R.C., 2001. Evidence for mantle metasomatism by hydrous silicic melts derived from subducted oceanic crust. *Nature* 410, 197–200. <https://doi.org/10.1038/35065583>.
- Putirka K., 2016. Amphibole thermometers and barometers for igneous systems and some implications for eruption mechanisms of felsic magmas at arc volcanoes. *American Mineralogist* 101 (4): 841–858. <https://doi.org/10.2138/am-2016-5506>
- Rapp R.P., and Watson E.B., 1995. Dehydration melting of metabasalt at 8–32 kbar: implications for continental growth and crust-mantle recycling. *Journal of Petrology* 36, 4, 891–931, <https://doi.org/10.1093/petrology/36.4.891>
- Rapp R.P., Shimizu N., Norman M.D., and Applegate G.S., 1999. Reaction between slab-derived melts and peridotite in the mantle wedge: experimental constraints at 3.8 GPa. *Chemical Geology* 160, 4, 335-356. [https://doi.org/10.1016/S0009-2541\(99\)00106-0](https://doi.org/10.1016/S0009-2541(99)00106-0)
- Reagan M.K., Ishizuka O., Stern R.J., Kelley J.A., Ohara Y., Blichert-Toft J., Bloomer S.H., Cash J., Fryer P., Hanan B.B., Hickey-Vargas R., Ishii T., Kimura J.-I., Peate D.W., Rowe M.C., and Woods M., 2010. Fore-arc basalts and subduction initiation in the Izu-Bonin-Mariana system, *Geochem. Geophys. Geosyst.*, 11, Q03X12, <https://doi.org/10.1029/2009GC002871>
- Reagan, M.K., McClelland, W.C., Girard, G., Goff, K.R., Peate, D.W., Ohara, Y., Stern, R.J., 2013. The geology of the southern Mariana fore-arc crust: implications for the scale of Eocene volcanism in the western Pacific. *Earth and Planetary Science Letters* 380, 41–51. <http://dx.doi.org/10.1016/j.epsl.2013.08.013>
- Renne, P.R., Balco, G., Ludwig, K.R., Mundil, R. and Min, K., 2011. Response to the comment by W.H. Schwarz et al. on "Joint determination of K-40 decay constants and Ar-40*/K-40 for the Fish Canyon sanidine standard, and improved accuracy for Ar-40/Ar-39 geochronology" by PR Renne et al. (2010). *Geochimica Cosmochimica Acta* 75, 5097-5100. <http://doi.org/10.1016/j.gca.2011.06.021>
- Richards J.P., and Kerrich R., 2007. Adakite-Like Rocks: Their Diverse Origins and Questionable Role in Metallogensis. *Economic Geology* 102, 4, 537–576. <https://doi.org/10.2113/gsecongeo.102.4.537>

- Rogkala A., Petrounias P., Tsikouras B., and Hatzipanagiotou K., 2017. New Occurrence of Pyroxenites in the Veria-Naousa Ophiolite (North Greece): implications on their origin and petrogenetic evolution. *Geosciences* 7(4), 92. <https://doi.org/10.3390/geosciences7040092>
- Sameshima, T., Paris, J.P., Black, P.M., and Heming, R.F., 1983. Clinoenstatite-bearing lava from Népoui, New Caledonia. *American Mineralogist* 68, 1076–1082.
- Saccani, E., Dilek, Y., and Photiades, A., 2018. Time-progressive mantle-melt evolution and magma production in a Tethyan marginal sea: a case study of the Albanide-Hellenide Ophiolites. *Lithosphere*, 10, 35–53. <https://doi.org/10.1130/L602.1>
- Secchiari A., Montanini A., Bosch D., Macera P., and Cluzel D. 2016. Melt extraction and enrichment processes in the New Caledonia lherzolites: evidence from geochemical and Sr-Nd isotope data. *Lithos* 260, 28-43. <https://doi.org/10.1016/j.lithos.2016.04.030>
- Secchiari A., Montanini A., Bosch D., Macera P., and Cluzel D., 2018. The contrasting geochemical message from the New Caledonia gabbro-norites: insights on depletion and contamination processes of the sub-arc mantle in a nascent arc setting. *Contributions to Mineralogy and Petrology* 173, 66. <https://doi.org/10.1007/s00410-018-1496-8>
- Secchiari A., Montanini A., Bosch D., Macera P., and Cluzel D., 2020. Sr, Nd, Pb and trace element systematics of the New Caledonia harzburgites: tracking source depletion and contamination processes in a SSZ setting. *Geoscience Frontiers* 11, 1, 37-55. <https://doi.org/10.1016/j.gsf.2019.04.004>
- Secchiari, A., Montanini, A., and Cluzel, D., 2022a. Temperatures and cooling rates recorded by the New Caledonia ophiolite: Implications for cooling mechanisms in young forearc sequences. *Geochemistry, Geophysics, Geosystems* 23, e2021GC009859. <https://doi.org/10.1029/2021GC009859>
- Secchiari, A., Montanini, A., and Cluzel, D., 2022b. Hydrous mafic–ultramafic intrusives at the roots of a proto-arc: implications for crust building and mantle source heterogeneity in young forearc regions. *Contributions to Mineralogy and Petrology* (2022) 177:50 <https://doi.org/10.1007/s00410-022-01912-x>
- Sécher, D., 1981. Les lherzolites ophiolitiques de Nouvelle-Calédonie et leurs gisements de chromite. Ph D. thesis, Université de Nantes, France, 228 p.
- Sevin B., Ricordel-Prognon C., Quesnel F., Cluzel D., and Maurizot P., 2012. First paleomagnetic dating of ferricrete in New Caledonia: new insight on the morphogenesis and paleoweathering of ‘Grande Terre’. *Terra Nova* 24, 77-85. <https://doi.org/10.1111/j.1365-3121.2011.01041.x>
- Schaen, A.J., et al., 2020. On the reporting and interpretation of $^{40}\text{Ar}/^{39}\text{Ar}$ geochronologic data, *Geological Society of America Bulletin* 133 (3-4), 461-487. <https://doi.org/10.1130/B35560.1>

- Shervais, J. W., Reagan, M. K., Haugen, E., Almeev, R., Pearce, J. A., Prytulak, J., et al., 2019. Magmatic response to Subduction Initiation, Part I: Fore-arc basalts of the Izu-Bonin arc from IODP Expedition 352. *Geochemistry, Geophysics, Geosystems*, 20/1, 314–338. <https://doi.org/10.1029/2018GC007731>
- Shervais, J. W., Reagan, M. K., Godard, M., Prytulak, J., Ryan, J. G., Pearce, J. A., et al., 2021. Magmatic response to subduction initiation, Part II: Boninites and related rocks of the Izu-Bonin Arc from IODP Expedition 352. *Geochemistry, Geophysics, Geosystems*, 22, e2020GC009093. <https://doi.org/10.1029/2020GC009093>
- Solovova, I.P., Ohnenstetter, D., Girnisa, A.V., 2012. Melt inclusions in olivine from the boninites of New Caledonia: post-entrapment melt modification and estimation of primary magma compositions. *Petrology* 20 (6), 529–544. <https://doi.org/10.1134/S0869591112060045>
- Soret, M., Agard, P., Dubacq, B., Vitale-Brovarone, A., Monié, P., Chauvet, A., Whitechurch, H., and Villemant, B., 2016. Strain localization and fluid infiltration in the mantle wedge during subduction initiation: Evidence from the base of the New Caledonia ophiolite, *Lithos* 244, 1-19. <https://doi.org/10.1016/j.lithos.2015.11.022>
- Soret M., Bonnet G., Agard P., Larson K.P., Cottle J.M., Dubacq B., Kylander-Clark A.R.C., Button M., Rividi N., 2022. Timescales of subduction initiation and evolution of subduction thermal regimes. *Earth and Planetary Science Letters* 584, 117521. <https://doi.org/10.1016/j.epsl.2022.117521>
- Spandler C., Rubatto D. and Hermann, J., 2005, Late Cretaceous–Tertiary tectonics of the southwest Pacific: insights from U–Pb sensitive, high resolution ion microprobe (SHRIMP) dating of eclogite facies rocks from New Caledonia: *Tectonics* 24, TC3003. <http://dx.doi.org/10.1029/2004TC001709>
- Steiger, R.H., and Jäger, E., 1977, Subcommittee on geochronology: Convention on the use of decay constants in geo- and cosmochemistry. *Earth and Planet. Sci. Lett.* 36, 359-362. [https://doi.org/10.1016/0012-821X\(77\)90060-7](https://doi.org/10.1016/0012-821X(77)90060-7)
- Stern R.J., 2004. Subduction initiation: Spontaneous and induced. *Earth and Planetary Science Letters* 226, 3-4, 275-292. <http://doi.org/10.1016/j.epsl.2004.08.007>
- Stern R.J., Reagan M., Ishizuka O., Ohara Y., and Whattam S., 2008. To understand subduction initiation, study forearc crust: To understand forearc crust, study ophiolites. *Lithosphere* 4, 6, 469–483. <http://doi.org/10.1130/L183.1>
- Sun, S.S., McDonough, W.I., 1989. Chemical and isotopic systematics of oceanic basalts: implications for mantle composition and processes. In: Saunders, A.D., et Norry, M.D. (Eds.), *Magmatism in the Ocean Basins*. Geological Society Special Publication 42, 313–345.
- Taetz S., Scherer E.E., Bröcker M., Spandler C., John T., 2021. Petrological and Lu-Hf age constraints for eclogitic rocks from the Pam Peninsula, New Caledonia. *Lithos* 388–389, 106073. <https://doi.org/10.1016/j.lithos.2021.106073>

- Taylor, J.R., 1982. An Introduction to Error Analysis: The Study of Uncertainties in Physical Measurements, Univ. Sci. Books, Mill Valley, Calif., 270 p.
- Taylor, J.R., 1982., An Introduction to Error Analysis: The Study of Uncertainties in Physical Measurements, Univ. Sci. Books, Mill Valley, Calif., 270 p.
- Taylor, W.R., 1998. An experimental test of some geothermometer and geobarometer formulations for upper mantle peridotites with application to the thermobarometry of fertile lherzolite and garnet websterite. *Neues Jahrbuch für Mineralogie - Abhandlungen* 172, 381-408. <https://doi.org/10.1127/njma/172/1998/381>
- Titus, S.J., Maes, S.M., Benford, B., Ferre, E.C. and Tikoff, B. 2011. Fabric development in the mantle section of a paleotransform fault and its effect on ophiolite obduction, New Caledonia. *Lithosphere*, 3, 221-244. <https://doi.org/10.1130/l122.1>
- Ulrich, M., Picard, C., Guillot, S., Chauvel, C., Cluzel, D., Meffre, S., 2010. Multiple melting stages and refertilisation process as indicators fort ridge to subduction formation: the New Caledonia ophiolite. *Lithos* 115, 223–236. <https://doi.org/10.1016/J.LITHOS.2009.12.011>
- Vermeesch, P., 2006. Tectonic discrimination diagrams revisited. *Geochemistry, Geophysics, Geosystems*, 7 (6), Q06017. <https://doi.org/10.1029/2005GC001092>
- Vitale Brovarone A. and Agard P., 2013. True metamorphic isograds or tectonically sliced metamorphic sequence? New high-spatial resolution petrological data for the New Caledonia case study. *Contrib Mineral Petrol* 166, 451–469. <https://doi.org/10.1007/s00410-013-0885-2>
- Vogt, J. and Podvin, P., 1983. Carte géologique à l'échelle du 1/50 000 et notice explicative: feuille Humboldt-Port-Bouquet. Territoire de Nouvelle-Calédonie - Bureau de Recherches Géologiques et Minières, Orléans, France, 1-68.
- Walker, D. A. , and Cameron, W. E., 1983. Boninite primary magmas: Evidence from the Cape Vogel Peninsula, PNG. *Contributions to Mineralogy and Petrology* 83, 1-2, 150-158. <http://doi.org/10.1007/BF00373088>
- Whattam, S. A., J. Malpas, J. R. Ali, and I. E. M. Smith, 2008. New SW Pacific tectonic model: Cyclical intraoceanic magmatic arc construction and near-coeval emplacement along the Australia-Pacific margin in the Cenozoic, *Geochem. Geophys. Geosyst.*, 9, Q03021. <http://doi.org/10.1029/2007GC001710>.
- Whattam, S.A. and Stern, R.J., 2011. The 'subduction initiation rule': a key for linking ophiolites, intra-oceanic forearcs, and subduction initiation. *Contributions to Mineralogy and Petrology* 162, 1031-1045. <https://doi.org/10.1007/s00410-011-0638-z>
- Winchester, J.A. and Floyd, P.A., 1977. Geochemical discrimination of different magma series and their differentiation product using immobile elements. *Chemical Geology*, 20, 325-343. [http://dx.doi.org/10.1016/0009-2541\(77\)90057-2](http://dx.doi.org/10.1016/0009-2541(77)90057-2)

- Wood, D. A., 1980. The application of a Th-Hf-Ta diagram to problems of tectonomagmatic classification and to establishing the nature of crustal contamination of basaltic lavas of the British Tertiary volcanic province. *Earth and Planetary Science Letters*, 50, 11-30.
[https://doi.org/10.1016/0012-821X\(80\)90116-8](https://doi.org/10.1016/0012-821X(80)90116-8)
- Wood B.J., and Turner S.P., 2009. Origin of primitive high-Mg andesite: Constraints from natural examples and experiments. *Earth and Planetary Science Letters* 283, 59–66.
<http://doi.org/10.1016/j.epsl.2009.03.032>
- Xiong Q., Zheng J.-P., Griffin W.L., O'Reilly S.Y., Pearson N.J., 2014. Pyroxenite dykes in orogenic peridotite from North Qaidam (NE Tibet, China) track metasomatism and segregation in the mantle wedge. *Journal of Petrology* 55, 12, 2347–2376.
<https://doi.org/10.1093/petrology/egu059>
- Xu Y., Liu C.-Z. and Lin W., 2021. Melt extraction and reaction in the forearc mantle: Constraints from trace elements and isotope geochemistry of ultra-refractory peridotites of the New Caledonia Peridotite Nappe, *Lithos* 380-381, 105882. <https://doi.org/10.1016/j.lithos.2020.105882>
- York, D., 1968. Least squares fitting of a straight line with correlated errors. *Earth and Planet. Sci. Lett.* 5, 320-324. [http://doi.org/10.1016/S0012-821X\(68\)8005](http://doi.org/10.1016/S0012-821X(68)8005)
- Yu, M., Dilek, Y., Yumul G.P. Jr, Yan, Y., Dimalanta C.B., Huang C.Y. (2020). Slab-controlled elemental–isotopic enrichments during subduction initiation magmatism and variations in forearc chemostratigraphy. *Earth and Planetary Science Letters*, 538, 116217.
<https://doi.org/10.1016/j.epsl.2020.116217>
- Zhang C., Holtz F., Koepke J., Wolff P.E., Ma C., Bédard J.H., 2013. Constraints from experimental melting of amphibolite on the depth of formation of garnet-rich restites, and implications for models of Early Archean crustal growth. *Precambrian Research* 231, 206-217.
<http://dx.doi.org/10.1016/j.precamres.2013.03.004>

Figure captions

Fig. 1: Geological sketch map of New Caledonia. BSZ: Belep Shear Zone, HC: Humboldt Corridor, BTF: Bogota Transform Fault. Inset, LHR: Lord Howe Ridge, NR: Norfolk Ridge, LR: Loyalty Ridge, HP: Hikurangi Plateau.

Fig. 2: Total Alkali-Silica diagram (Le Bas et al., 1986; Le Maitre et al., 2002) to show the diversity in composition of Lower Eocene dykes. The rock nomenclature is mainly field-based; some discrepancies may be due to element mobility.

Fig. 3: Plum pyroxenite intrusion. (a) Geological map redrawn from the online geological map of New Caledonia, (www.georep.nc); (b) and (c) Tectonic sketch of transcurrent (dextral) emplacement of Plum intrusion and satellite dykes. (b) First step, transtensional intrusion of the main body. (c) Second step, passive rotation and emplacement of new shear-parallel dykes.

Fig. 4: Whole-rock geochemical features of Plum and Ouassé pyroxenites, Nepoui boninite and boninite-series felsic dykes (a) Chondrite-normalized REE diagram (Evensen et al., 1978) for Plum pyroxenite (a), Ouassé pyroxenite (c) and boninite-series dykes (e); the dotted pattern represents the dated sample ($^{40}\text{Ar}/^{39}\text{Ar}$). (b) MORB-normalized REE and trace elements spiderdiagram (Sun and McDonough, 1989) for Plum pyroxenite (b), Ouassé pyroxenite (d) and boninite-series dykes (f). Dotted patterns refer to dated samples (U-Pb zircon). REE and REE-Tr diagrams for Népoui boninite (Cluzel et al., 2016) and modeled melts for pyroxenites of Plum (Secchiari et al., 2022b) and Ouassé (Ferrari, 2021) are shown for comparison.

Fig. 5: $^{40}\text{Ar}/^{39}\text{Ar}$ data for the amphiboles of the Plum samples; PL-AM7 pyroxenite and PL-AM10 hornblende-gabbro dyke. (a, b) show the age spectra, K/Ca and radiogenic yield diagrams obtained by the incremental heating experiments and (c,d) are the isochron diagrams. The isochron ages are the preferred cooling ages of the samples.

Fig. 6: Geological map of Bogota Peninsula (redrawn from the online geological map of New Caledonia, www.georep.nc)

Fig. 7: $^{40}\text{Ar}/^{39}\text{Ar}$ degassing diagram for the amphiboles of Ouassé pyroxenite dykelets.

Fig. 8: Chondrite-normalized REE diagrams (Evensen et al., 1978) and MORB-normalized REE and trace elements spiderdiagrams (Sun and McDonough, 1989) for hornblende-bearing dykes, anorthosites and granites: a-b, hornblendites; c-d hornblende-rich gabbros/diorites, e-f, "anorthosites", g-h granites. (a) and (b) dashed patterns represent dated samples (Ar/Ar); (c) and (d) blue patterns represent dated samples (U-Pb zircon); (e) and (f), dashed patterns represent dated samples (U-Pb zircon); (g) and (h) plain lines type 1 granites, dashed lines type 2 granites.

Fig. 9: Whole-rock geochemical features of dolerite dykes. (a) Classification diagram of Winchester and Floyd (1977), most samples plot in the field of andesitic basalts; the white triangle represents the sample #DMBE 3 (IAB-like) and the purple dot represents the andesite dredge sample from IPOD progral. (b) Chondrite-normalized REE diagram (Evensen et al., 1978); the bold dotted pattern represents #SIR 8 dated at 50.4 Ma ($^{40}\text{Ar}/^{39}\text{Ar}$). (c) Ternary Hf-Th-Ta "discriminant" diagram (Wood 1980; Vermeesch, 2006) most samples plot in the island-arc tholeiite (IAT) domain. (d) MORB-normalized REE and trace elements spiderdiagram (Sun and McDonough, 1989) same patterns as (b).

Fig. 10: $^{40}\text{Ar}/^{39}\text{Ar}$ age spectrum diagram diagram for the dolerite SIR 8 (Si Reis nickel mine, Boulinda Massif).

Fig. 11: Nd-Sr isotope ratios of selected Lower Eocene dykes and HT amphibolites of the metamorphic sole

Fig. 12: Sr/Y vs. Y discrimination diagram (Defant and Drummond, 1990) to show that about 60% of dykes have low Y contents and Sr/Y ratios >20 and thus correspond to adakite-like rocks (Richards and Kerrich, 2007). Note that only about 20% of dykes plot in the domain of adakite sensu stricto, these likely were issued from a source containing a significant amount of garnet.

Fig. 13: Slab melt modeling. (a) REE-Tr spiderdiagrams of HT amphibolites of the metamorphic sole (Cluzel et al., 2012b) taken as a protolith for slab melt modeling (Zhang et al., 2013). (b) Spiderdiagrams of modeled melts through 20-40% partial melting of amphibolites (green array) compared with the array of hornblende-diorite/gabbro dykes (hatched) and dated dykes (black lines).

Fig. 14: (a) simplified evolution of the Eocene subduction zone, from inception to slab steepening. (b) sketch model of shallow-dipping hot subduction to show the location of high-temperature amphibolites of the metamorphic sole and relationships between oblique subduction, development

of shear zones and exhumation of the mantle wedge. (c) sketch diagram of fluid and melt circulations in the mantle wedge between 55 and 50 Ma.

Supplementary figures (Appendix)

Suppl. Fig. S1: columnar section of New Caledonia Ophiolite, mainly based on the Montagne des Sources sequence (Massif du Sud).

Suppl. Fig. S2: Field pictures. (a) moderately sheared hornblende-gabbro dyke crosscutting websterite (Plum intrusion); (b) foliated websterite (Plum intrusion); (c) HT sheared harzburgite with shallow-dipping stretching lineation (Ouassé Bay, Bogota Shear Zone); (d) pyroxenite dykelets crosscutting sheared harzburgite (Ouassé Bay); (e) boudinaged pyroxenite (white arrow, Ouassé Bay). Smyl= mylonitic foliation.

Suppl. Fig. S3: Field pictures. (a) anastomosed hornblendite dykes (N'go Pass); (b) weathered hornblende-gabbro dyke crosscutting Plum pyroxenite; (c) mylonitized hornblende-gabbro dyke (Plum); (d) mylonitized hornblende-gabbro dyke with eye-shaped hornblendite porphyroclast (Plum); (e) incipient hornblendite/anorthosite layering (composite dyke, Ouen Island); (f) isoclinally folded anorthosite/hornblendite internal layering, white arrow: anthophyllite rim around a peridotite ghost enclave (gabbro dyke, Ouen Island); (g) hornblendite enclaves in a hornblende-gabbro dyke (Ouen Island); (h) co-magmatic anorthosite and hornblende-rich enclaves in the same dyke (Ouen Island).

Suppl. Fig. S4: MgO-SiO₂ and MgO-TiO₂ diagrams for boninite classification (Pearce and Reagan, 2019). Abbreviations: BA= basaltic andesite, LOTI= low-Ti basalts, SHMB= high-Mg basalts, HMA= high-Mg andesite, BADR= basalt-andesite-dacite-rhyolite suite, LSB= low-Si boninites, HSB= high-Si boninites.

Suppl. Fig. S5: (a) Terra-Wasserburg U-Pb zircon diagram for RPYR 6 hornblendite; (b) ⁴⁰Ar/³⁹Ar age spectrum diagram for VOH 1 hornblendite

Suppl. Fig. S6: Terra-Wasserburg U-Pb zircon diagrams of twelve selected hornblende gabbros/diorites.

Suppl. Fig. S7: Terra-Wasserburg U-Pb zircon diagrams of one anorthosite (a) and four selected granites (b).

Suppl. Fig. S8: Whole-rock geochemical features of Haute Néhoué andesites. (a) Classification diagram of Winchester and Floyd (1977), most samples plot in the field of andesite. (b) Chondrite-normalized REE diagram (Evensen et al., 1978); the bold dashed pattern in a and b represents #NHE 10 diorite dyke dated at 54.7 ± 0.8 Ma (U-Pb zircon). (c) MORB-normalized REE and trace elements spiderdiagram (Sun and McDonough, 1989)

Suppl. Fig. S9: Tectonic sketch to illustrate the two possible interpretations of high-temperature shear zones of Peridotite Nappe. 3a: transform fault model; 3b: C-C' shears model

Suppl. Fig. S10: Evolution of some elemental ratios during the 57-48 Ma period. Note the absence of evolution of Mg# and Sr/Y (most other ratios not presented); in contrast, there is a neat increase of Th/Ta ratio and Nb negative anomaly through time.

Suppl. Fig. S11: (a) age-latitude relationships of Lower Eocene dykes based upon conventional U-Pb zircon ages only. Note the small age difference of ca. 1 myr between south-easternmost and north-westernmost dykes. Errors in latitude have been arbitrarily taken as 0.01° ; (b) sketch diagram of the Eocene subduction zone shortly after inception to account for southward age progression of forearc activity (for clarity, curvature at that stage is somewhat exaggerated).

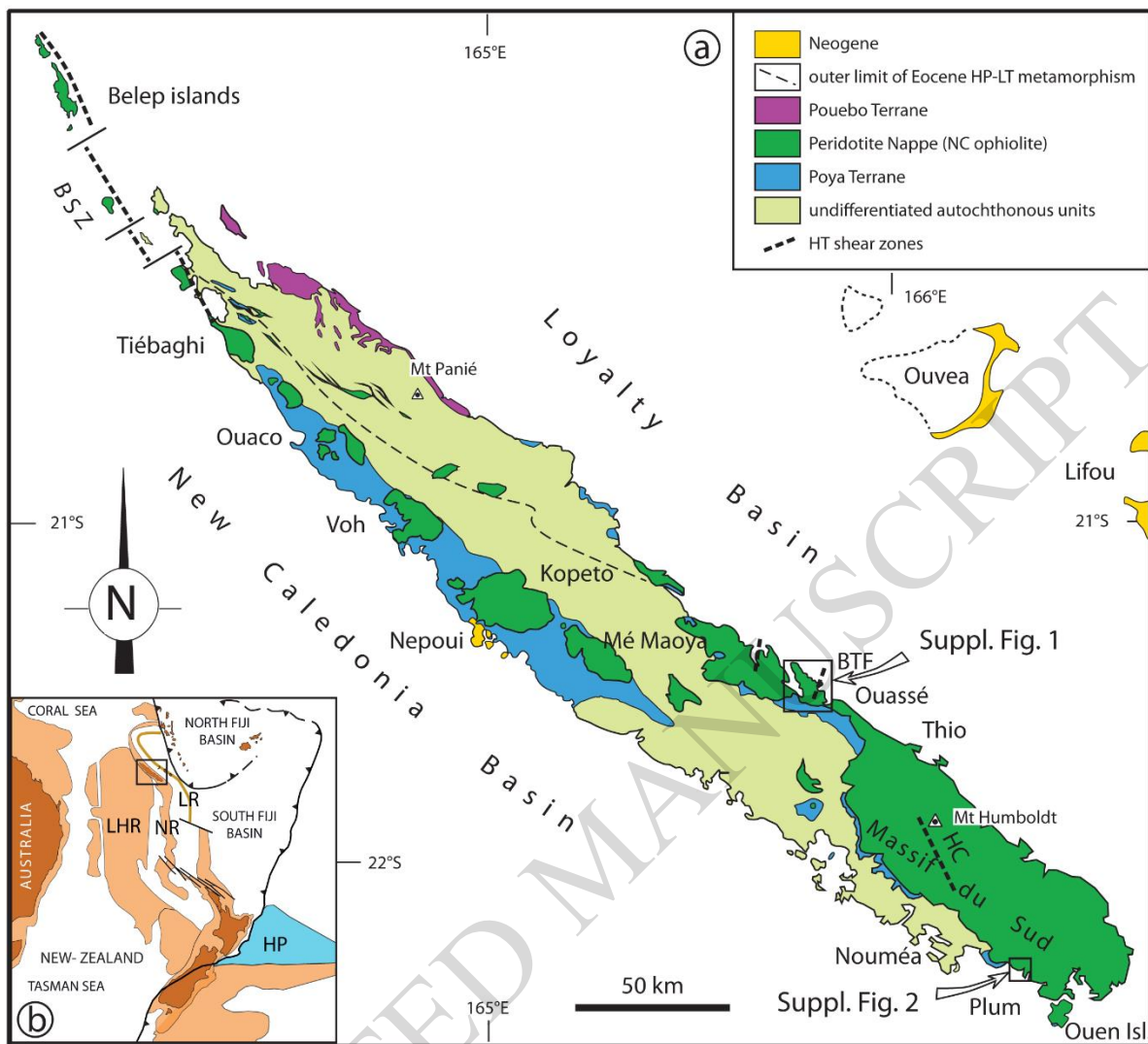


Figure 1

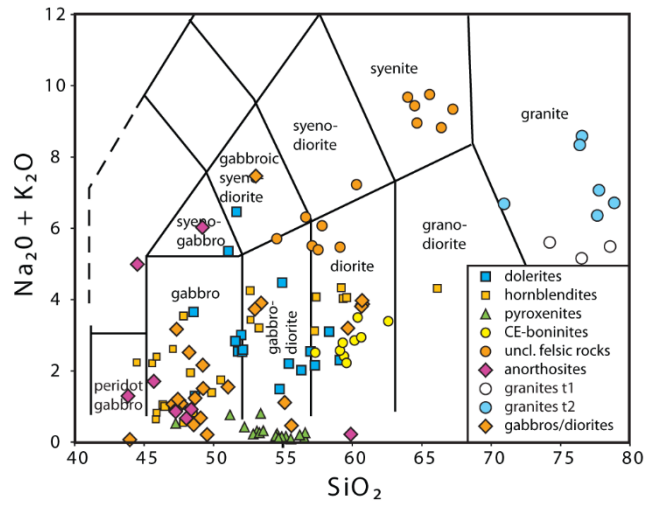


Figure 2

ACCEPTED MANUSCRIPT

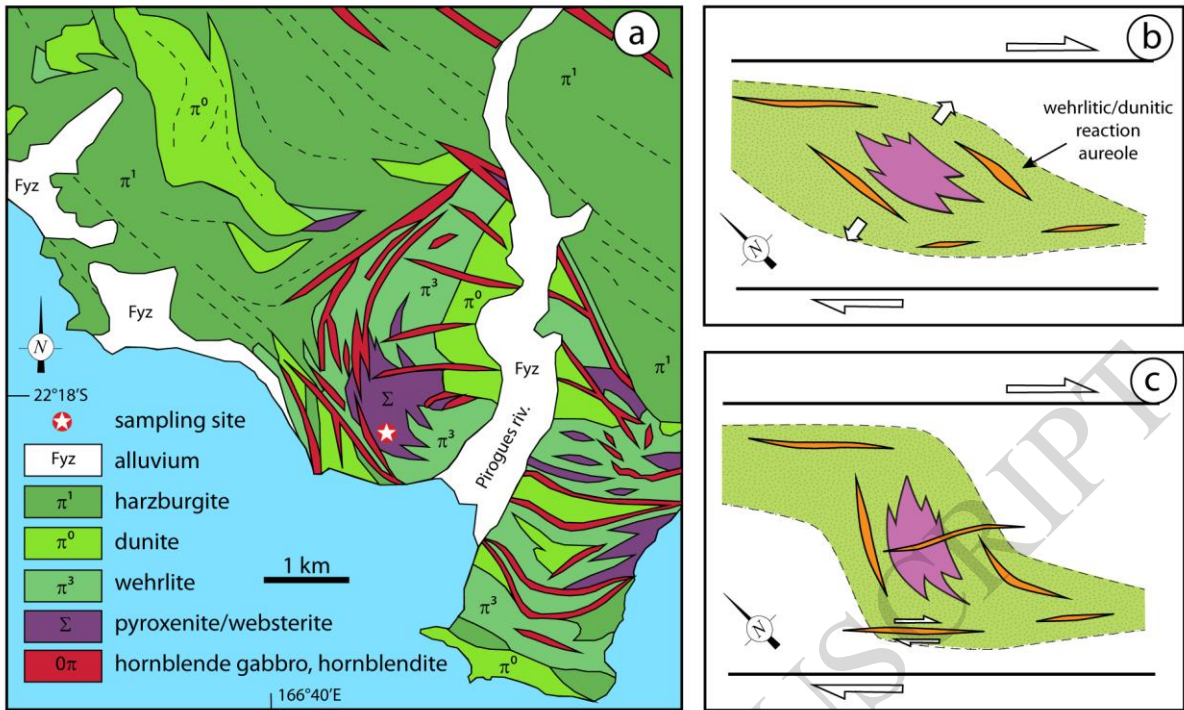


Figure 3

ACCEPTED MANUSCRIPT

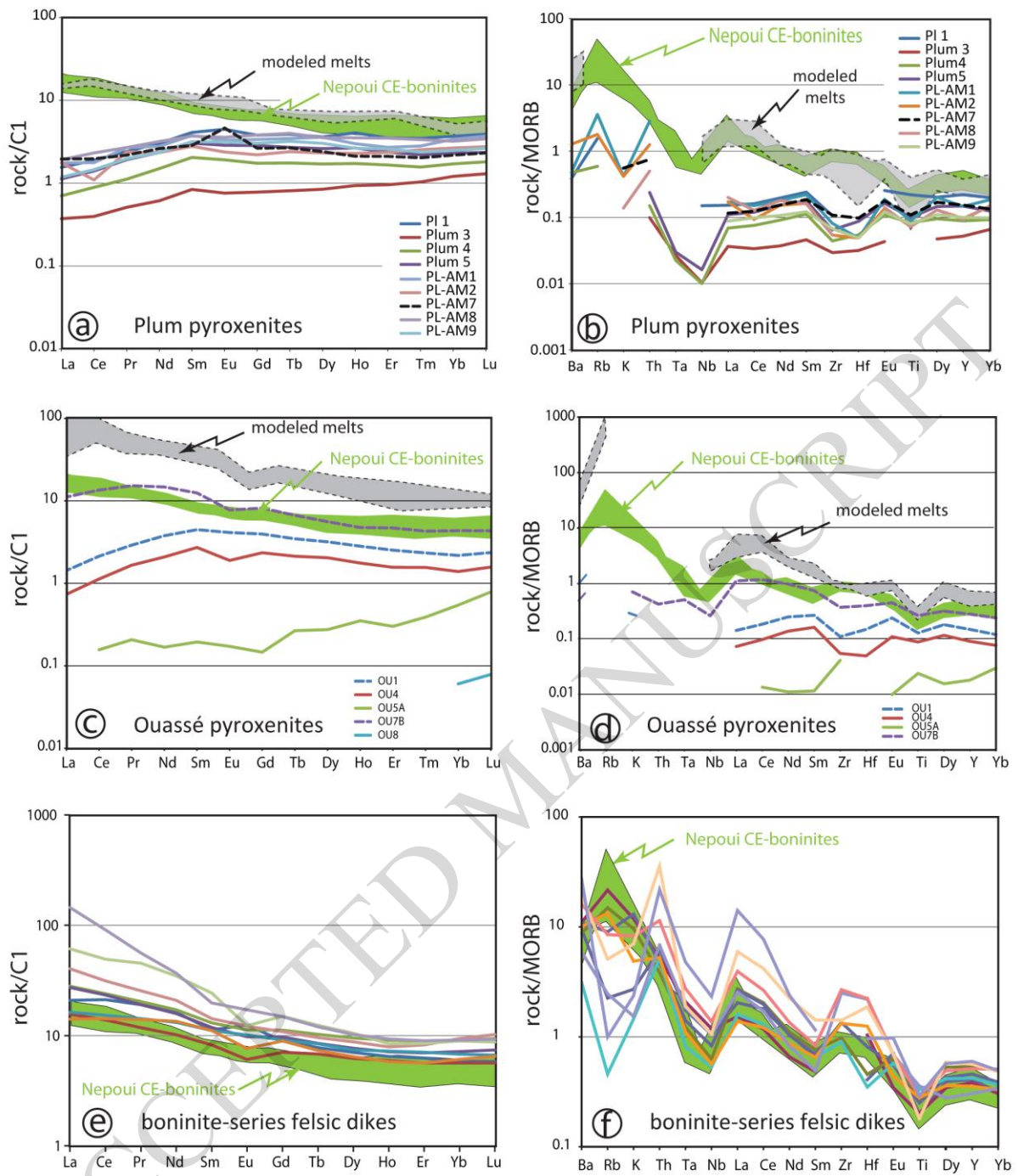


Figure 4

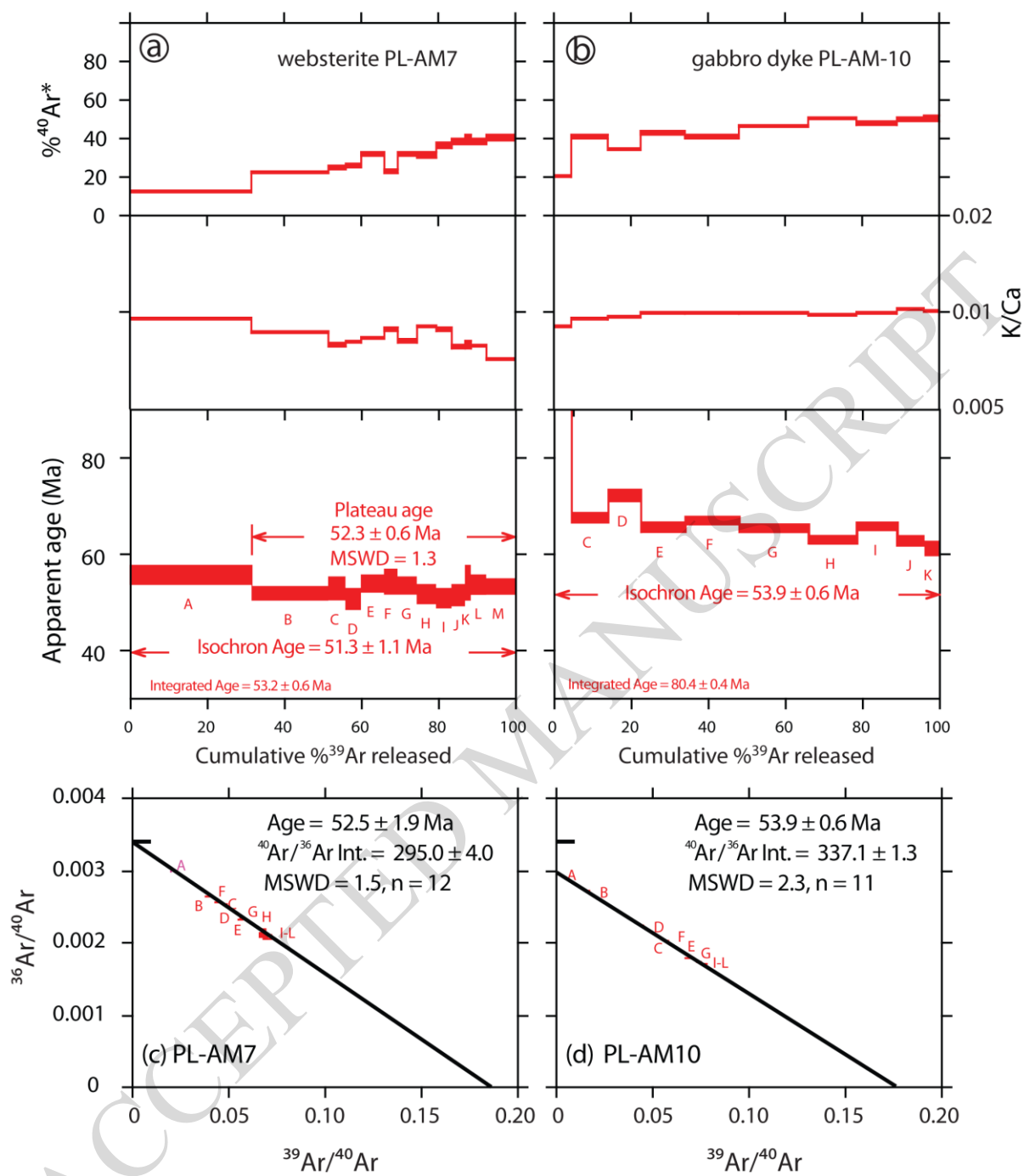


Figure 5

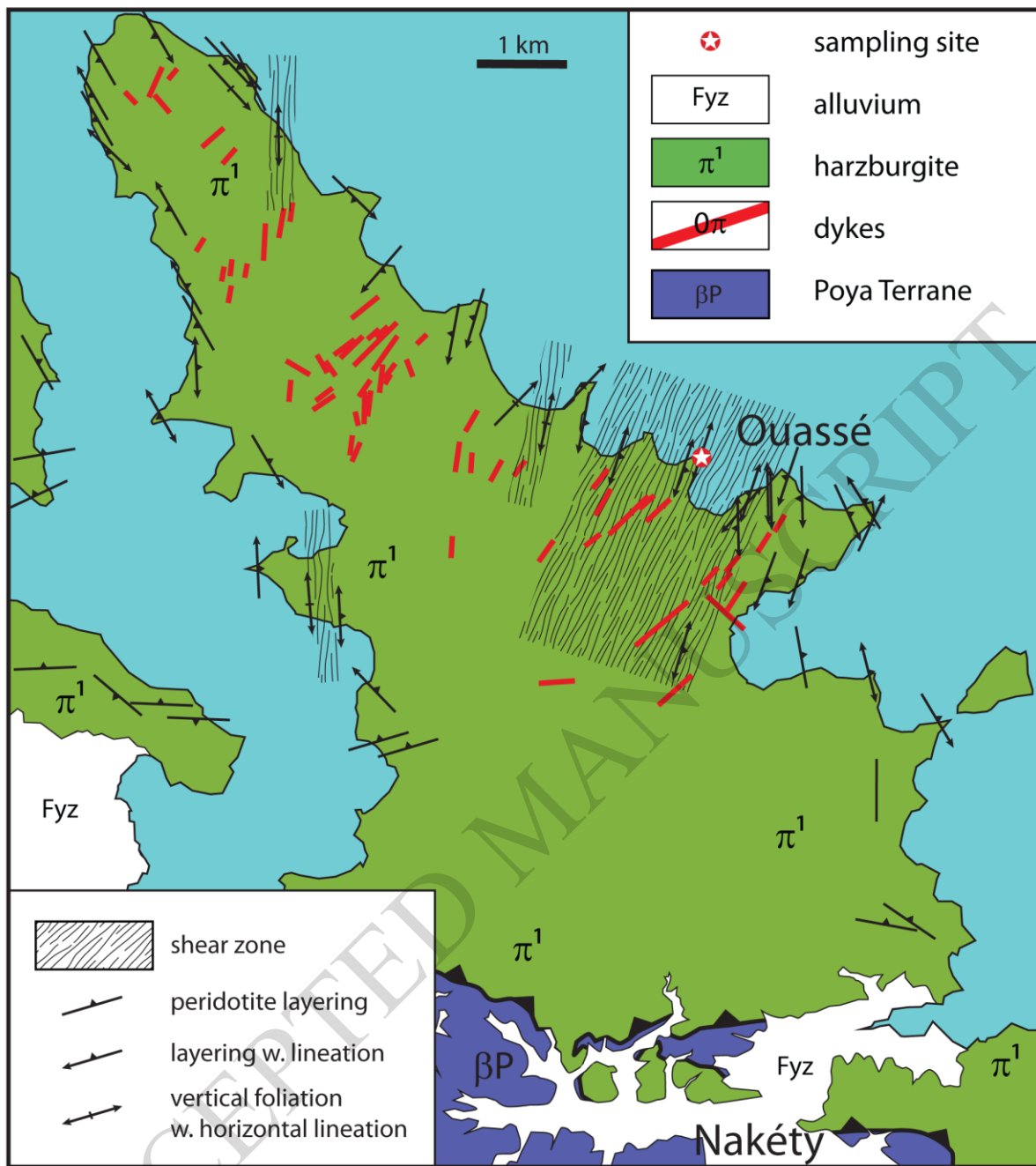


Figure 6

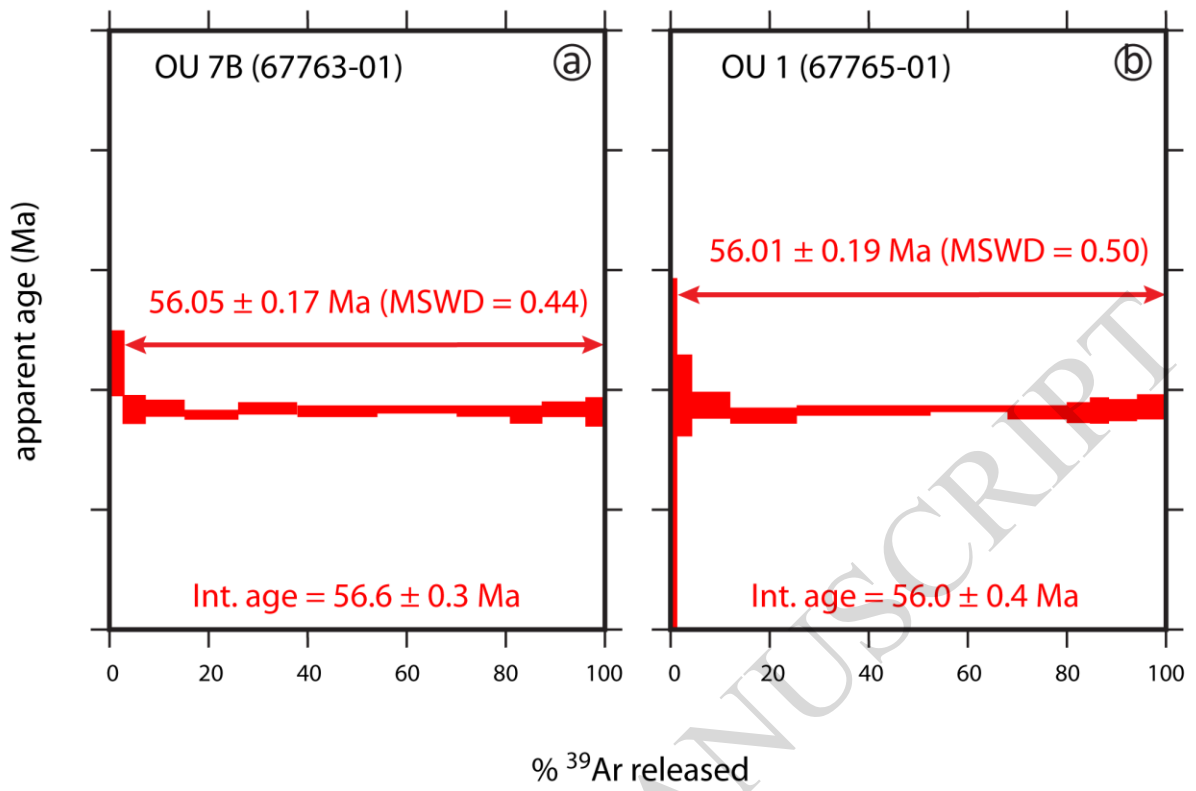


Figure 7

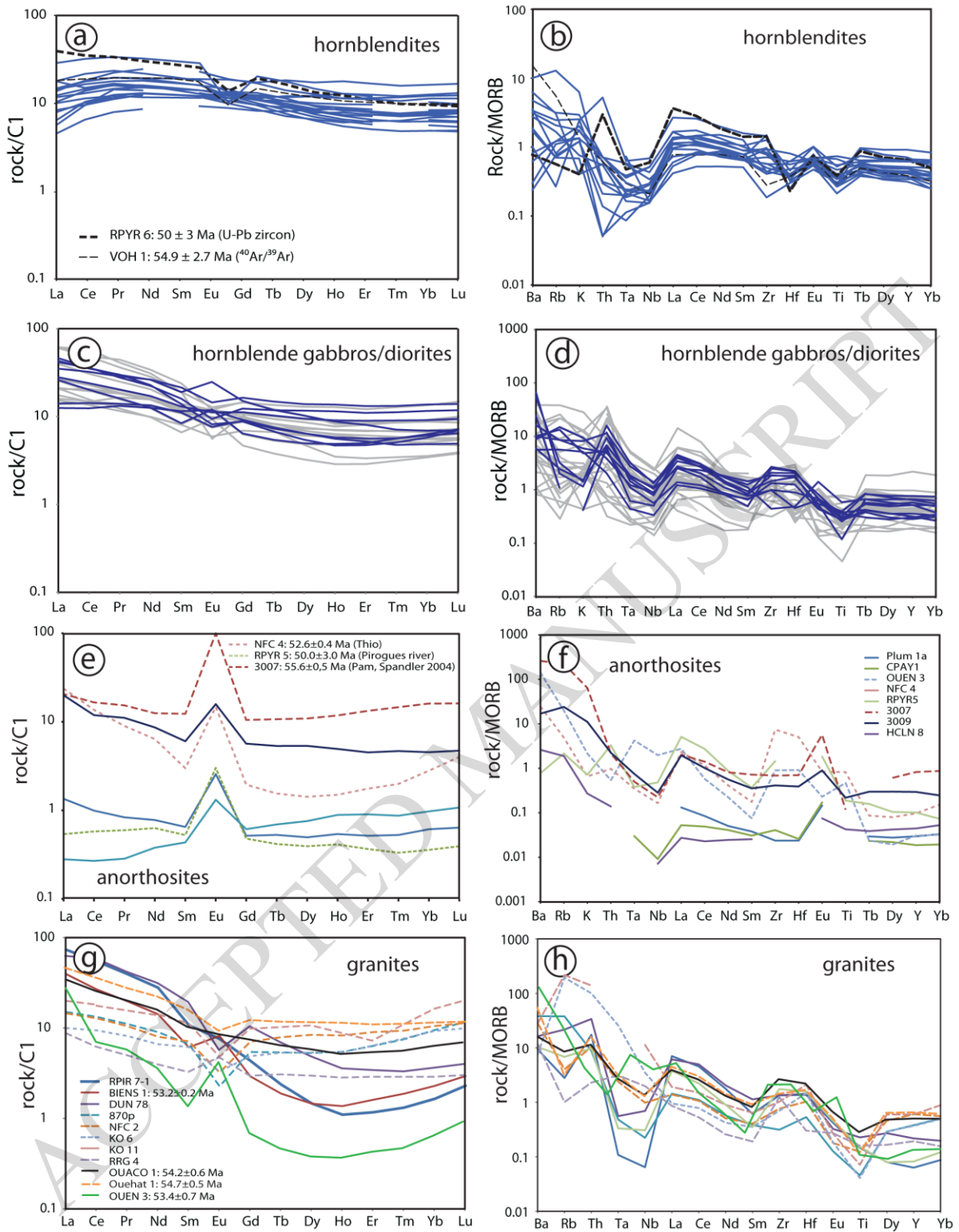


Figure 8

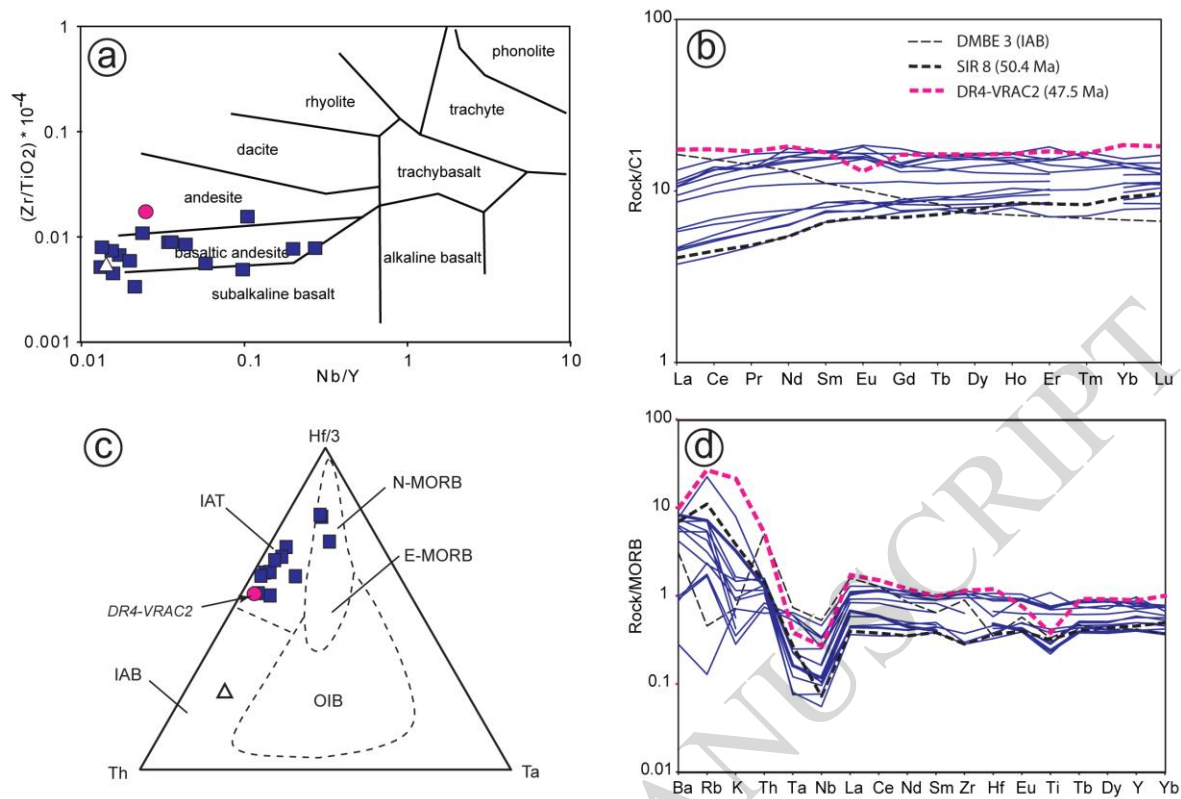


Figure 9

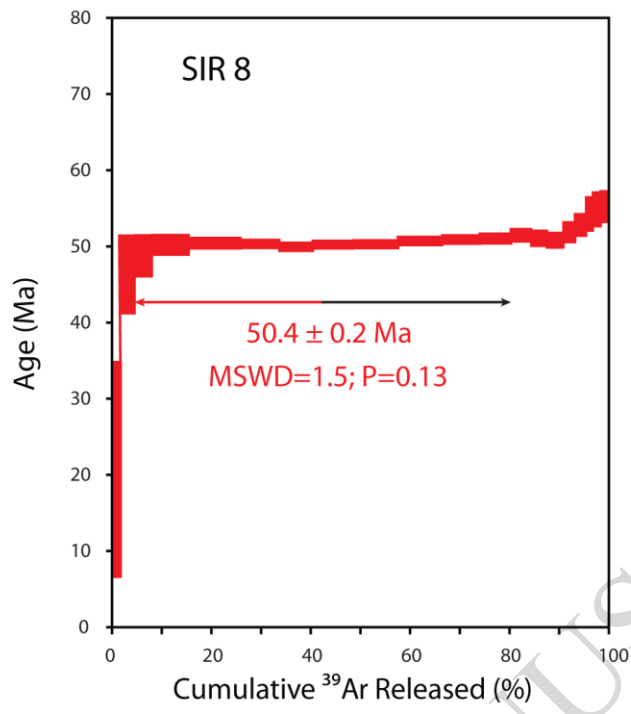


Figure 10

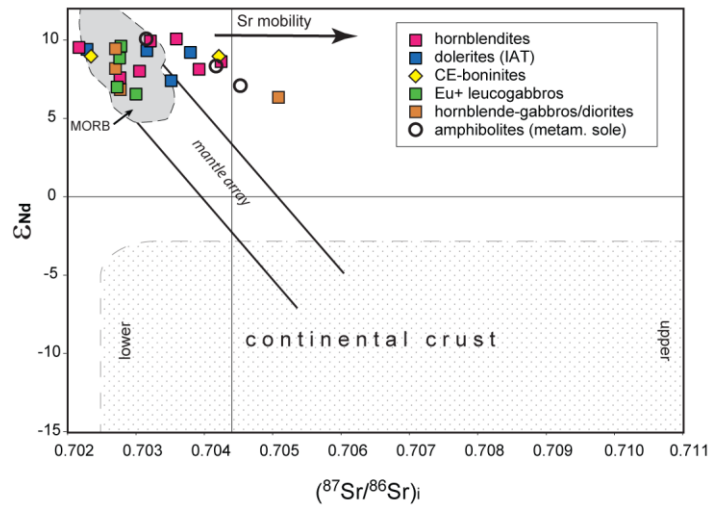


Figure 11

ACCEPTED MANUSCRIPT

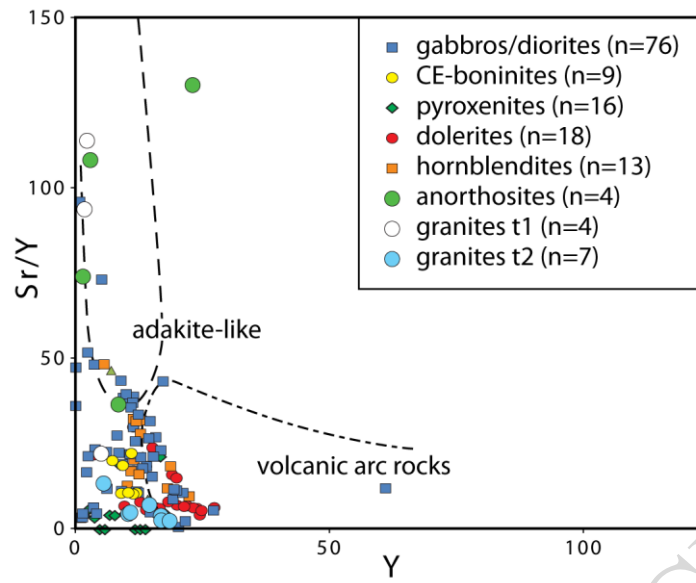


Figure 12

ACCEPTED MANUSCRIPT

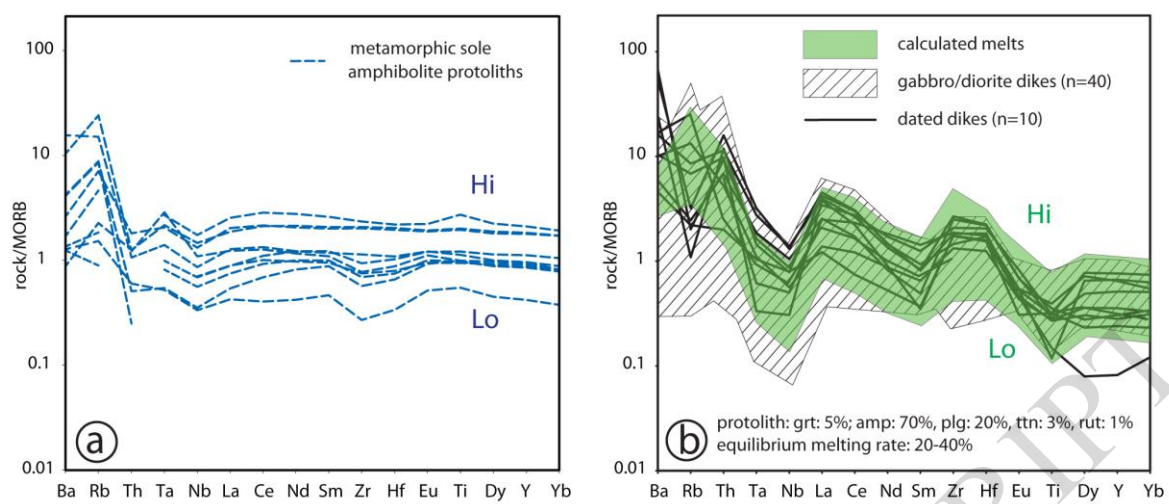


Figure 13

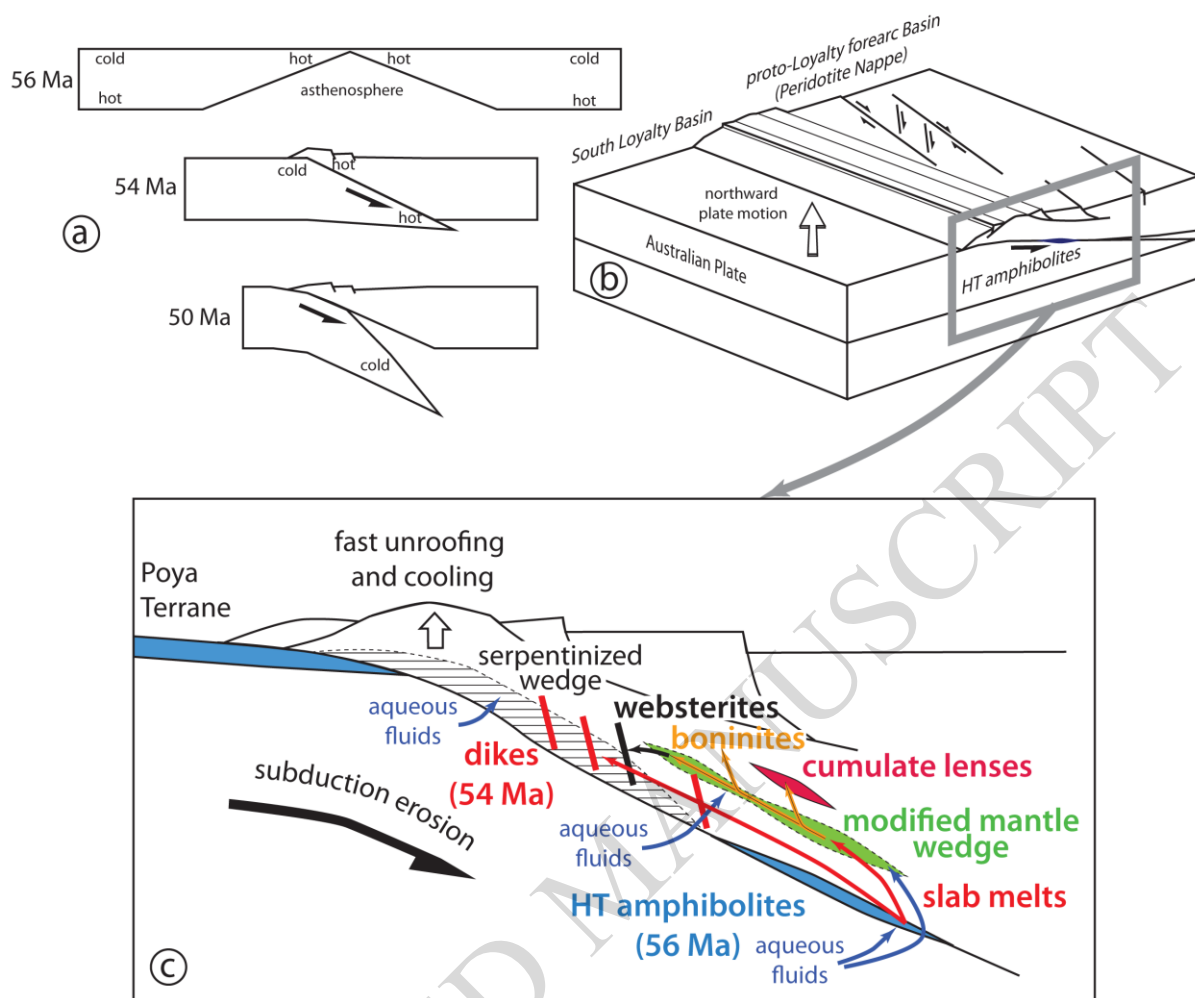


Figure 14